

UNIVERSITY OF CALIFORNIA
RIVERSIDE

Measurement of Identified Charged Hadron Elliptic Flow in $\sqrt{s_{NN}} = 200$ GeV
d+Au collisions

A Dissertation submitted in partial satisfaction
of the requirements for the degree of

Doctor of Philosophy

in

Physics

by

Matthew Mendoza

September 2016

Dissertation Committee:

Dr. Richard Seto , Chairperson

Dr. Kenneth Barish

Dr. Robert Clare

Copyright by
Matthew Mendoza
2016

The Dissertation of Matthew Mendoza is approved:

Committee Chairperson

University of California, Riverside

Acknowledgments

I am grateful to my advisor, without whose help, I would not have been here.

To my parents for all the support.

ABSTRACT OF THE DISSERTATION

Measurement of Identified Charged Hadron Elliptic Flow in $\sqrt{s_{NN}} = 200$ GeV d+Au collisions

by

Matthew Mendoza

Doctor of Philosophy, Graduate Program in Physics
University of California, Riverside, September 2016
Dr. Richard Seto , Chairperson

It is well known that the novel state of matter known as the Quark Gluon Plasma (QGP) created at the Relativistic Heavy Ion Collider (RHIC) suppresses high transverse momentum jets. A study of the baryon-to-meson production ratio in Au+Au collisions has shown a clear increase in the intermediate pT region for central Au+Au collisions indicative of the production of a QGP. PHENIXs Time of Flight detector, used in conjunction with the Aerogel Cherenkov Counter, can provide particle identification with good proton/meson separation for $p_T < 10$ GeV/c. I will present studies of particle identified two particle production using these detectors in a di-jet correlation analysis which could help to elucidate the underlying physics of the baryon excess anomaly.

Contents

| | |
|--|-----------|
| List of Figures | ix |
| List of Tables | xi |
| 1 Introduction | 1 |
| 1.1 Introduction | 1 |
| 1.2 Early Experiments: An Overview | 3 |
| 2 Nuclear Matter: Hot and Cold | 6 |
| 2.1 Hot versus Cold Nuclear Matter | 6 |
| 2.2 The Cronin Effect | 6 |
| 2.2.1 Initial State Multiple Scattering | 8 |
| 2.2.2 Final State Multiple Scattering | 10 |
| 2.3 Hot Nuclear Matter: QGP | 12 |
| 2.3.1 Baryon Enhancement | 13 |
| 2.3.2 Theoretical Models of Baryon Enhancement | 13 |
| 2.4 Flow at the LHC | 17 |
| 2.5 Recombination and Fragmentation for All? | 18 |
| 3 Experimental Apparatus | 22 |
| 3.1 The Relativistic Heavy Ion Collider | 22 |
| 3.2 From Start to Finish | 23 |
| 3.3 The PHENIX Detector | 25 |
| 3.3.1 Central Arm | 25 |
| 3.3.2 Forward and Global Detectors | 39 |
| 4 Heavy Ion Collisions: A Primer | 44 |
| 4.1 Measurable Quantities | 44 |
| 4.2 Event Characterization | 45 |
| 4.2.1 Centrality | 45 |
| 4.2.2 Event Vertex and Timing | 47 |
| 4.3 Track Reconstruction | 49 |
| 4.3.1 Variables for Track Selection | 49 |
| 4.3.2 Particle Identification | 49 |

| | | |
|----------|---|-----------|
| 4.4 | Nuclear Modification Factor | 52 |
| 5 | Anisotropic Flow | 54 |
| 6 | Event Plane | 57 |
| 6.1 | Determination of Event Plane | 57 |
| 6.2 | Event Plane "Flattening" | 57 |
| 6.3 | Event Plane Resolution Correction | 57 |
| 7 | Results | 58 |
| 7.1 | Charged Track v_2 | 58 |
| 7.2 | Separating Particle Signals | 58 |
| 7.2.1 | Single Gaussians | 58 |
| 7.2.2 | Gaussian Mixing | 58 |
| 7.2.3 | ACC as a Pion Discriminator | 58 |
| 7.3 | Yield vs Event Plane | 58 |
| 7.4 | Identified Particle v_2 | 58 |
| 8 | Error Analysis | 59 |
| 8.1 | Systematic Errors | 59 |
| 9 | Summary and Conclusions | 60 |
| 9.1 | Discussion | 60 |
| 9.2 | Conclusions | 60 |
| A | PHENIX Coordinate System | 61 |

List of Figures

| | | |
|------|--|----|
| 2.1 | Proton vs pion yield ratio from the Cronin paper | 7 |
| 2.2 | Illustration of Initial State Multiple Scattering | 8 |
| 2.3 | Feynman diagram of Drell-Yan production of dileptons. | 9 |
| 2.4 | Planarity of jets created with protons incident on Pb targets vs H targets. . | 11 |
| 2.5 | Illustration of Final State Multiple Scattering | 12 |
| 2.6 | Evidence of Baryon Enhancement in Au+Au collisions | 14 |
| 2.7 | Recombination model compared with Au+Au data | 16 |
| 2.8 | Illustration of an example hard scatter resulting in fragmentation to two pions | 17 |
| 2.9 | Elliptic Flow in p+Pb at the LHC | 18 |
| 2.10 | p/π ratios compared for central d+Au and peripheral Au+Au | 19 |
| 2.11 | Pion transverse momentum distribution from d+Au collisions compared to one created with the recombination model | 20 |
| 3.1 | An Aerial view of BNL | 22 |
| 3.2 | Illustration of all the accelerators used to boost ions to relativistic speeds at RHIC | 23 |
| 3.3 | PHENIX Detector Configuration for RHIC Run 8 (2008) | 26 |
| 3.4 | Wire net configuration in the DC | 28 |
| 3.5 | Schematic of the Pad Chambers | 30 |
| 3.6 | A schematic of the slat layout in the TOFE | 31 |
| 3.7 | An illustration of a single slat in the TOFE | 32 |
| 3.8 | Diagram of a basic RPC | 33 |
| 3.9 | Cross sectional diagram of the MRPCs used in the TOFW | 34 |
| 3.10 | A schematic of the Aerogel Cherenkov Counter | 35 |
| 3.11 | A schematic of one tile in the ACC | 36 |
| 3.12 | Chart of Particle Identification capabilities over a range of transverse mo- mentum | 37 |
| 3.13 | A diagram of the RICH | 38 |
| 3.14 | Schematics of EMCal components | 40 |
| 3.15 | The Beam Beam Counter | 41 |
| 3.16 | Centrality bins as determined by ZDC energy versus BBC charge sum . . . | 42 |
| 3.17 | Schematic of the MPC | 43 |

| | | |
|-----|--|----|
| 4.1 | Spectators and participant nucleons in a heavy ion collision | 46 |
| 4.2 | Central versus peripheral ion collisions | 47 |
| 4.3 | Diagram of BBC event characterization | 48 |
| 4.4 | Particle separation in the TOF | 50 |
| 4.5 | m^2 vs p_T showing clear constant separation of particle signatures. | 52 |
| 5.1 | Plots of the first four harmonics of a cosine series | 56 |
| A.1 | PHENIX coordinate system | 61 |

List of Tables

Chapter 1

Introduction

1.1 Introduction

Mankind has always striven to understand the universe around it. From the deepest distances of outer space to the infinitesimally small structures of the atoms that comprise the matter we interact with everyday, our understanding of the intricacies of our world has revealed such amazing complexities, many of which we have harnessed the power of in order to better ourselves and our quality of life. Over the last century, one such exploration that has uncovered many unforeseen phenomena is the study of the building blocks of matter and the forces that hold it together. From Planck's discovery that the world of the incredibly small is not smooth and continuous but rather comprised of discrete quanta, extending to Bohr's model of the atom showing that even the orbital dynamics of electrons were non classical, to the discovery of the neutron leading the way to the discovery of new fundamental forces of nature, field theories to describe them, and eventually the venerable standard model of particle physics, our ever increasing understanding of the workings of the atom

has revealed many discoveries that were surprising to those who sought them. In the last few decades one such investigation into the makings of the atomic nucleus seeks to study the properties of this nuclear material under temperature and density extrema, namely the search for phenomena where quarks and gluons that make up a solid phase of nuclear matter like protons and neutrons in a nucleus would become deconfined and melt into a novel state of matter called the *Quark Gluon Plasma* (QGP) at said extrema. First discussions of this deconfinement were found when Collins and Perry [15] said that at small distances the coupling constant would decrease implying that dense nuclear matter would comprise of deconfined quarks and gluons. Though their inferences pertained to low temperature, high density systems, they noted that similar phenomena could occur in high temperature systems like that of the early universe. The first to coin the term "Quark-Gluon Plasma" was Shuryak in 1980 [37] who wrote:

"When the energy density ϵ exceeds some typical hadronic value ($\sim 1 \text{ GeV/fm}^3$), matter no longer consists of separate hadrons (protons, neutrons, etc.), but as their fundamental constituents, quarks and gluons. Because of the apparent analogy with similar phenomena in atomic physics we may call this phase of matter the QCD (or quarkgluon) plasma."

With this theoretical framework, we have set out to develop an understanding of this phase transition whose resulting deconfinement of quarks and gluons has led to a new era of physics discoveries.

1.2 Early Experiments: An Overview

The earliest experiments that utilized collisions of two ions to study nuclear matter were largely repurposing existing accelerators that were used for elementary particle physics. Whereas the general goal of an accelerator setup to study elementary particle physics is to study the production of exotic single particles created in specific Quantum Field Theory processes (baryons, mesons, force carrier bosons, leptons) an accelerator used for Heavy Ion Physics is used to study larger nuclear matter systems which result in higher track multiplicity consisting of particles created by more common processes.

Examples of this include the repurposing of the weak focusing proton synchrotron called the Bevatron at Lawrence Berkeley National Laboratory when it was joined with the SuperHiLac, a linear accelerator capable of accelerating ions to relativistic energies of up to 2 GeV per nucleon and became the only machine in the world capable of accelerating all of the elements in the periodic table to relativistic speeds. This capability allowed researchers to pioneer the study of "quark matter" [23] the crowning achievement of this epoch being the discovery that nuclear matter could be compressed to high temperature [36], made evident by the observation of collective flow in Niobium + Niobium ions at 400 MeV/nucleon [24] which paved the way for the search for other phases of nuclear matter, namely the Quark Gluon Plasma.

The first step into the "ultra-relativistic" energy regime (> 10 GeV/nucleon) took place at Brookhaven National Lab in the mid 80's with the Alternating Gradient Synchrotron which initially was able to reach 14 GeV per nucleon with Silicon ions. Concurrently across the ocean, the European Organization for Nuclear Research (Conseil European

pour la Recherche Nuclaire, CERN) had the Super Proton Synchrotron accelerated Oxygen and Sulfur ions up to 200 GeV per nucleon. By the mid 90's both had seen their own upgrades that allowed them to create larger systems with the use of so called "Heavy" ions. At the AGS, Gold ions accelerated to 11 GeV per nucleon, and at the SPS, Lead ions accelerated to 158 GeV per nucleon[41]. Both accelerators set the stage for RHIC, each with their own prolific periods of discovery.

At the AGS, the observation of directed and elliptic flow in 11.5 GeV Au + Au collisions at the AGS by the E877 collaboration [9] showed that quark matter behaved collectively, that it was indeed a new state of matter not just a conglomerate of independent nuclei. The E802 collaboration compared the production of charged kaons compared to charged pions in 14.6 GeV Si + Au collisions and saw the "strange" result that the production of kaons was enhanced compared to proton + proton collisions showing that the collective behavior of this quark matter produced a different spectrum of particles than the simpler p + p collisions [1].

At the SPS, this strangeness enhancement was also studied by the NA49[26] collaboration through a similar measurement of the charged kaon to pion ratio and the WA97[8] collaboration measuring the production of multistrange baryons ($\Lambda, \bar{\Lambda}, \Xi^\pm$, and Ω^\pm). Meanwhile the NA50 collaboration was finding not enhancement but suppression of J/Ψ mesons (which decay to $l^+ + l^-$ pairs) when compared to $l^+ + l^-$ pairs created through Drell-Yan processes (see fig 2.3) [3].

Concurrently, the teams at the two accelerators used two particle correlations to study the evolving collision volume and saw that the energy density of the quark matter

was considerably higher, an order of magnitude greater, than naturally stable laboratory nuclei [25] and found the conditions for thermal freeze out [11], i.e. the reconfinement of quarks and gluons into hadronic states, a process called *hadronization*.

These various phenomena were signatures of new physics that could not be explained by solely scaling up $p + p$ collisions, they were signs that the nuclear material had undergone a transformation, more specifically, a phase transition and a sign of quark-gluon deconfinement.

Chapter 2

Nuclear Matter: Hot and Cold

2.1 Hot versus Cold Nuclear Matter

Because the deconfinement corresponds to a condition where the temperature of the system is above some critical temperature it is often called "Hot Nuclear Matter." Therefore, the region of the nuclear matter phase diagram where quarks and gluons are confined to baryon and meson states is often called "Cold Nuclear Matter." Historically, "Hot" QGP systems were those created by colliding two large nuclei such as in Au+Au collisions and "Cold Nuclear Matter" systems were made by colliding large nuclei with smaller ones such as in d+Au collisions and in beam collisions with fixed nuclear targets.

2.2 The Cronin Effect

The seminal paper titled **Production of hadrons at large transverse momentum at 200, 300, and 400 GeV** by J.W. Cronin, et al. detailed a fixed target

experiment that collided protons with a tungsten target and underpinned a phenomenon found in cold nuclear matter systems. Later dubbed the *Cronin Effect* after the paper's first author, the experiment found that the production of protons at mid p_T ($2 \leq p_T \leq 4$) was enhanced when compared to the production of pions [17].

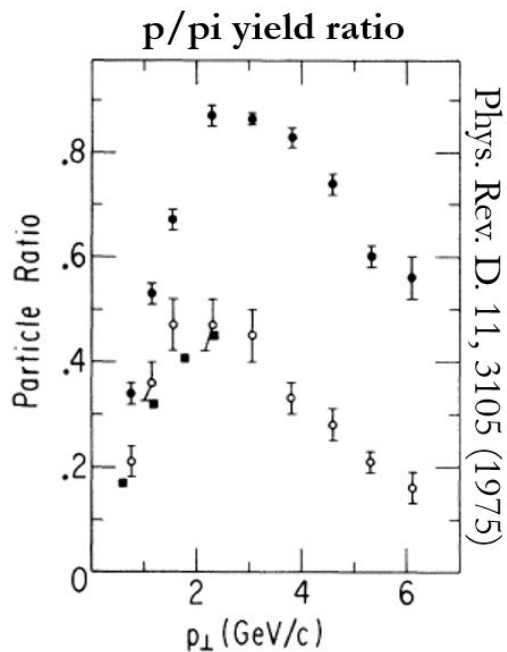


Figure 2.1: Proton vs pion yield ratio from the Cronin paper. Closed circles are the ratio obtained by colliding $23.7 \text{ GeV}/c^2$ protons on tungsten ($A=110$). Open circles are the same data extrapolated ($A=1$).

After this discovery many set out to come up with theoretical mechanisms that could explain this baryon production preference. These mechanisms can largely be categorized into two types: those where the incoming partons interact with the nuclear medium

and those where outgoing partons created after an incoming nucleon hard scatters interacts with the nuclear medium. These two categories are called *Initial State Interactions* and *Final State Interactions*.

2.2.1 Initial State Multiple Scattering

The first attempts at explaining the Cronin Effect were made using initial state interactions. Kohn in 1975 described a mechanism where incoming quarks scatter with nuclear quarks which randomize the direction of the incoming parton before finally colliding with another quark to produce an event similar to a proton-proton collision[31]. Since it is unclear how many "soft scatters" happen before the final hard scatter the p_T spectrum is broadened which could account for the increase of particle production for the mid p_T range.

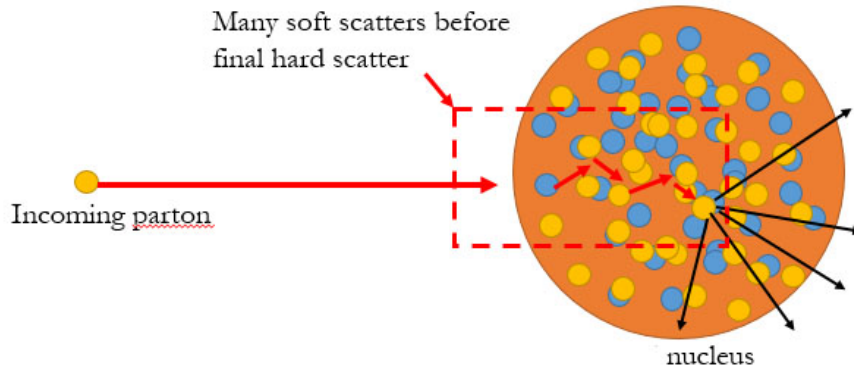


Figure 2.2: Illustration of Initial State Multiple Scattering.

The NA10 collaboration at CERN set out to use back to back lepton probes to

study the effect of the nucleus on jets. They collided 140 GeV and 258 GeV negative pions on tungsten targets of various thicknesses and looked for muon pairs produced via a Drell-Yan Process.

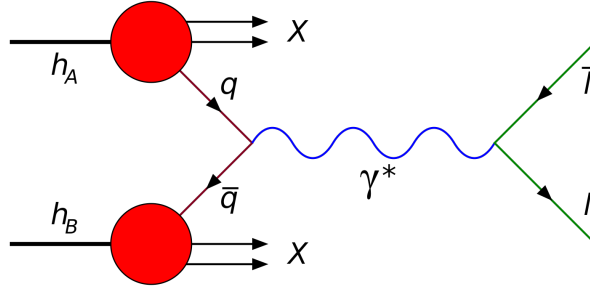


Figure 2.3: Feynman diagram of Drell-Yan production of dileptons. Quark-Antiquark annihilation produces a lepton-antilepton pair through the exchange of a virtual photon.[18]

They found that the mean squared p_T did not vary much at all as a function of target thickness which implies that incident partons are not affected by the thickness of the target and therefore that the path length of soft collisions that would broaden the p_T spectrum is very short. Furthermore, the E772 collaboration, with an experiment colliding 800 GeV protons on H_2 , C, Ca, Fe, and W targets, showed that Drell-Yan produced dileptons mean squared p_T did not vary much between the nuclear targets of varying nucleon number.[7] i.e. increasing the number of nucleons does not change the net p_T much, further showing that initial state contributions to p_T broadening is minimal.

2.2.2 Final State Multiple Scattering

In 1991 the E609 collaboration at Fermilab studied dijets produced in fixed target experiments colliding 400 GeV/c protons with targets made of various nuclear materials including hydrogen and lead[16]. The conditions of interest to them were the creation of two back to back jets produced after an incoming parton hard scattered with a target nucleon. They defined a quantity called *planarity* which measured how *back-to-back* two jets are. In their words:

”An axis is found which maximizes the sum of the squares of all momentum components (b_{max}) along that axis while minimizing the sum of the squares of momentum components perpendicular to that axis (b_{min}). Planarity is then defined as:

$$P = \frac{b_{max} - b_{min}}{b_{max} + b_{min}}. \quad (2.1)$$

For two narrow back-to-back jets P approaches 1, while for a circularly symmetric event P is 0.”

Their measurement compared the planarity of dijets created from protons colliding with a hydrogen target with the planarity of those created with collisions on a lead target. They noticed a downward shift in planarity and broadening of the spectrum for Pb dijets compared to H although both had very similar jet widths. This measurement led to a paper in 1993 where they concluded that Parton hard scatterings within nuclei involve very little nuclear scattering of the incident parton, but that there is substantial nuclear rescattering of outgoing hard scattered partons.[20] Because of this, we call this type of mechanism a *Final State Interaction*. While it is true that this could account for the increase in particle

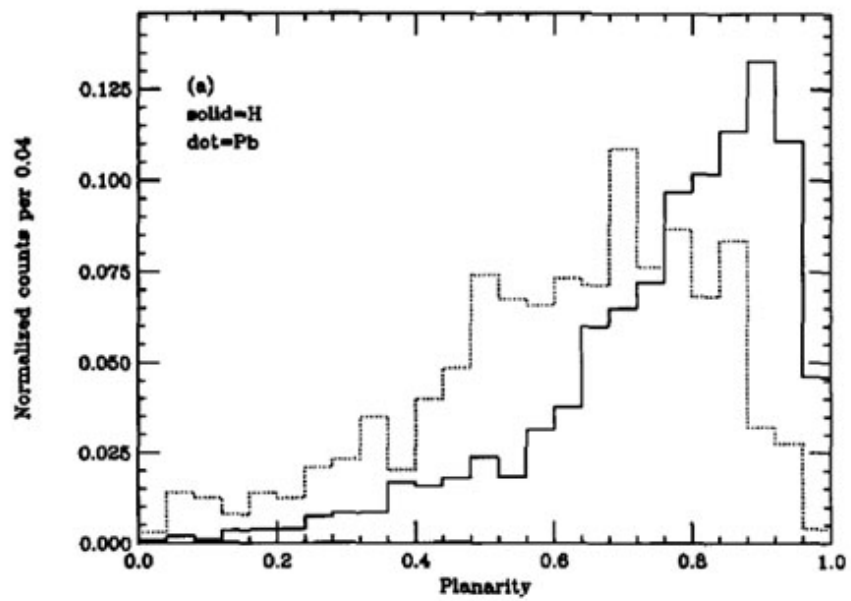


Figure 2.4: Planarity of jets created with protons incident on Pb targets vs H targets.

production it does not effectively explain why the effect is stronger for baryons than for mesons and why this preference disappears for at high p_T

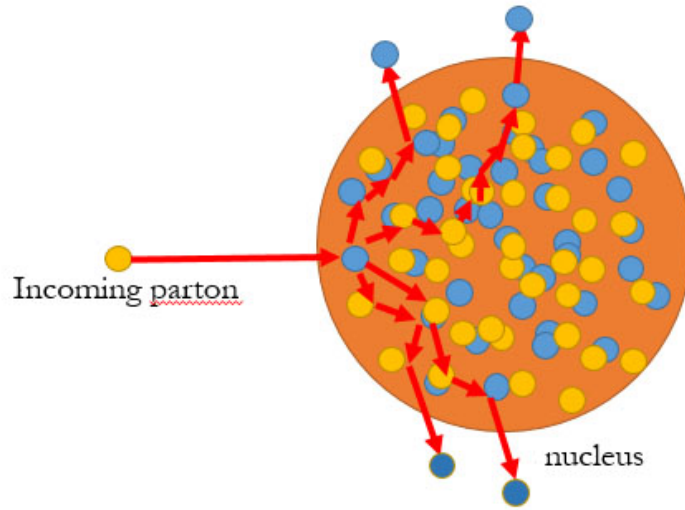


Figure 2.5: Illustration of Final State Multiple Scattering.

2.3 Hot Nuclear Matter: QGP

So far this discussion has stayed within the temperature regime where quarks and gluons are confined to hadronic states. As summarized in the previous chapter, physicists had already seen enough hints that new physics was taking place when the energy density reached some critical value and consequently RHIC was commissioned to study this phase change.

2.3.1 Baryon Enhancement

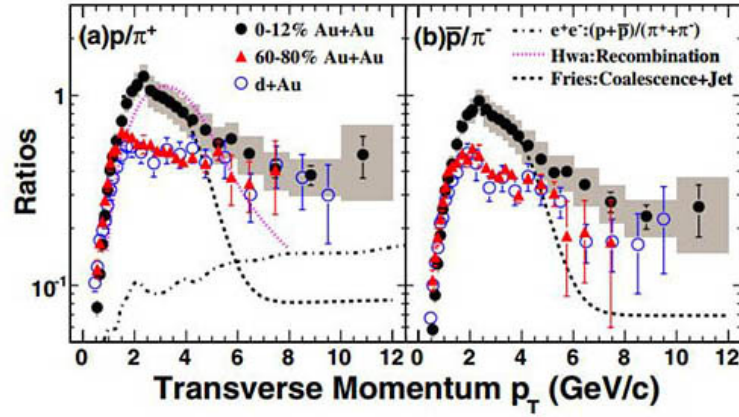
One of the surprises encountered when studying this new phase of matter was that the production of particles seemed to have a different mechanism compared to p+p collisions. One experimental signature of this was the so called *baryon enhancement* for peripheral Au+Au collisions [2]. This result is shown in figure 3.15a which shows the comparative yield between protons and pions in bins of p_T . The phenomena of interest is the apparent baryon excess in central collision data set for the mid p_T range which is strongest at around $p_T \approx 2$ GeV/c and disappears at around $p_T \approx 4$ GeV/c. Similarly, the Nuclear Modification factor for Central and Peripheral collisions also shows this enhancement in the same range (shown in figure 3.15b).

2.3.2 Theoretical Models of Baryon Enhancement

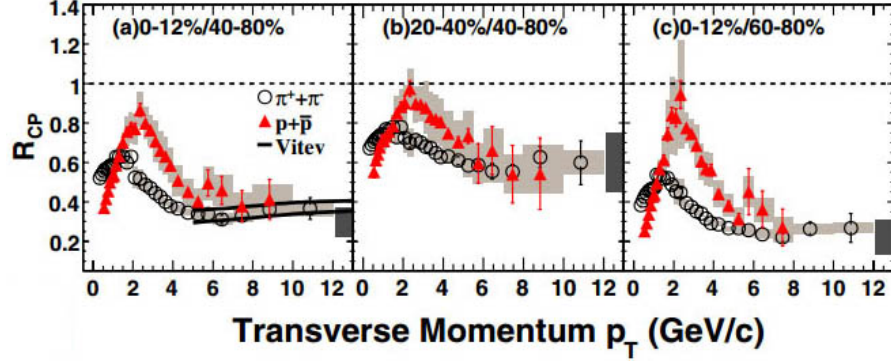
Though many have proposed models to describe this baryon enhancement, I will focus this discussion on the two leading models.

Recombination

Following the idea that a phase change in nuclear matter happens when a critical energy density causes deconfinement of quarks and gluons from their bound states as neutrons and protons and that the post-collision evolutionary behavior of this QGP is one that expands rapidly, Rudolph Hwa and C.B. Yang postulated that the enhancement of particle production could be explained by the ways in which the outgoing partons interacted[28]. They defined two types of partons, those with low transverse momentum created by the



(a) p/π^+ and \bar{p}/π^- ratios for central and peripheral 200 GeV Au+Au collisions. Two leading models are compared to the data as well as the same ratio for 200 GeV d+Au collisions.



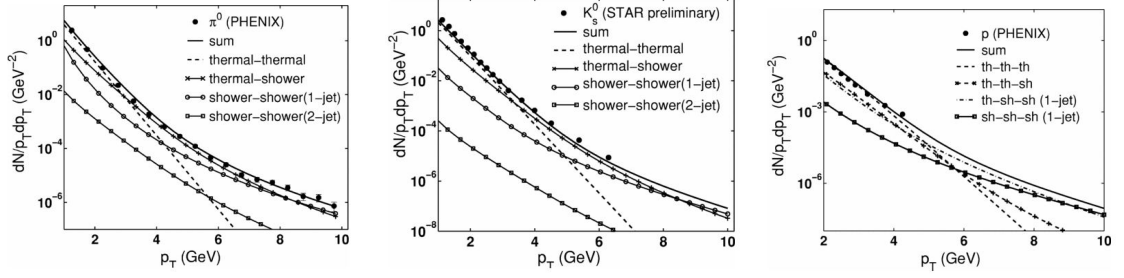
(b) Nuclear modification factor, R_{CP} , comparing nuclear effects on particle production in central versus peripheral Au+Au collisions compared to production in binary scaled p+p collisions

Figure 2.6: p/π production ratio and R_{CP} as evidence of Baryon Enhancement in central Au+Au

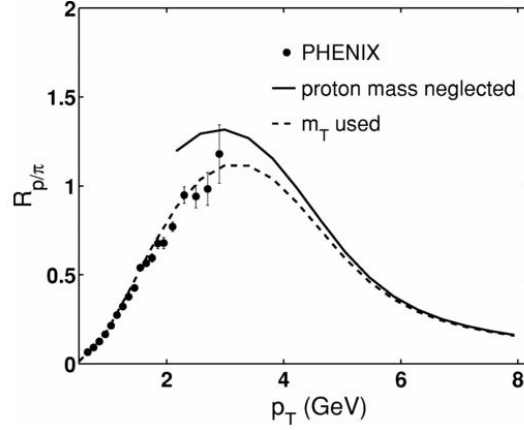
hydrodynamic outward expansion of the QGP referred to as *soft* and/or *thermal* partons and those with high transverse momentum created by *hard* nuclear scattering processes or *shower* partons. The production of particles could then be described by the way these partons combined combinatorically, i.e. the way thermal partons combined with other thermal partons, the way they combined with shower partons, and the way shower partons combined with other shower partons. This mechanism was termed *recombination* since it relied on the recombining of quarks in partons created from the nuclear collision.

Fragmentation

Fries, Mueller, Nonaka, and Bass postulated that the the reason why protons were produced in abundance was simply that following a collision, the building blocks of protons: up and down quarks, are plentiful and that they simply recombine back into their confined states. This mechanism dominates for low p_T since outgoing partons are traveling slowly which allows the constituent quarks to remain connected by a color string. In contrast to the soft thermal partons, partons created with hard scattering processes are more likely to break the color string creating quark/anti-quark pairs, i.e. mesons. Because this range of p_T causes individual quarks in the QGP to fragment out, the lone quarks scatter off with enough energy to create quark antiquark pairs from the vacuum which pair up with the nuclear quarks . This two regime model naturally creates a baryon preference for low p_T partons that is met with proportional meson production when the parton p_T is adequately high enough.



(a) p_T distribution of pions (b) p_T distribution of kaons (c) p_T distribution of protons



(d) p/π production ratio versus p_T

Figure 2.7: Au+Au identified particle measurements compared with recombination model predictions. For the p_T distributions we see three distinct regions of recombination, the low p_T range where soft thermal parton recombination dominates, the high p_T range where hard shower parton recombination dominates, and the middle range where thermal-shower recombination best describes the data.

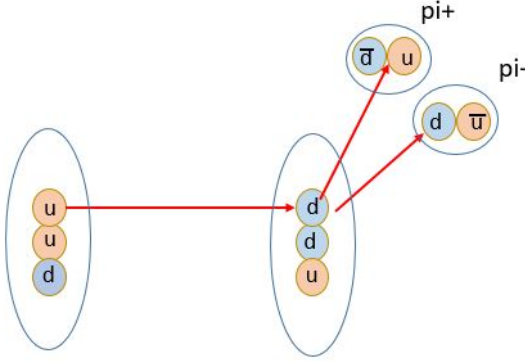


Figure 2.8: Illustration of an example hard scatter resulting in fragmentation to two pions. Here an up quark scatters with enough energy to scatter and release the down quark from being bound in another nucleon. This occurs with enough energy to create antiparticle partners from the vacuum resulting in the formation of charged pions.

2.4 Flow at the LHC

Up till now it appeared that the lines in the proverbial sand were clear with respect to nuclear matter phase changing and that we had two distinct ways to measure the properties of these two states. There is cold hadronic matter which has its own experimental signatures that are measured with beam on fixed target experiments and with small ion (protons and deuterons) on heavy ion collisions and hot deconfined quark matter which flows and behaves another way and studied using collisions of two heavy nuclei. This notion that the two experimental methods allowed the temperature dependent phenomena to be studied separately was brought into question in 2015 when the Large Hadron Collider (LHC) at CERN turned on and entered its second era of measurements. At the Compact

Muon Solenoid (CMS) they collected data from p+Pb collisions at 5.02 TeV and compared it to Pb+Pb collisions at 2.76 TeV. While hydrodynamic phenomena like collective flow was expected in the Pb+Pb data, they found the unexpected when a nonzero elliptic flow was measured in p+Pb (see fig 2.9).

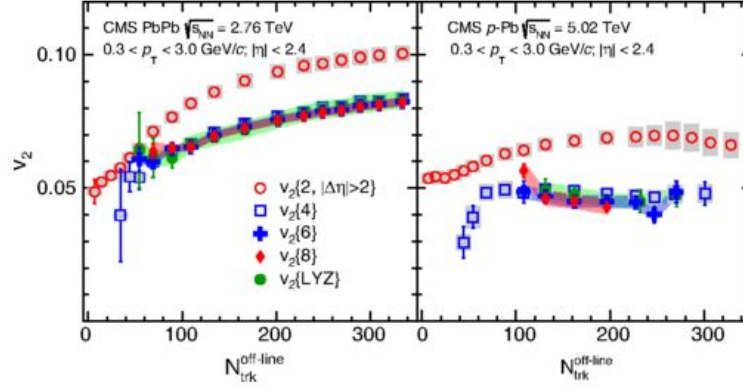


Figure 2.9: CMS result from 5.02 TeV p+Pb collisions showing a nonzero elliptic flow signal versus track multiplicity

The appearance of flow in systems previously thought of as "cold" was a sign that perhaps the QGP forms much easier than previously expected and that perhaps some phenomena found in cold systems, such as baryon enhancement, could be attributed to mechanisms that found favor in explaining similar phenomena in hot heavy ion systems.

2.5 Recombination and Fragmentation for All?

Furthermore, experimental evidence that the two systems behave quite similarly has been found. In fig. 2.11 particle production ratios (p/π) are compared and we see that

the baryon enhancement which was indicative of the QGP formation in peripheral Au+Au collisions is followed extremely closely by data from central d+Au.

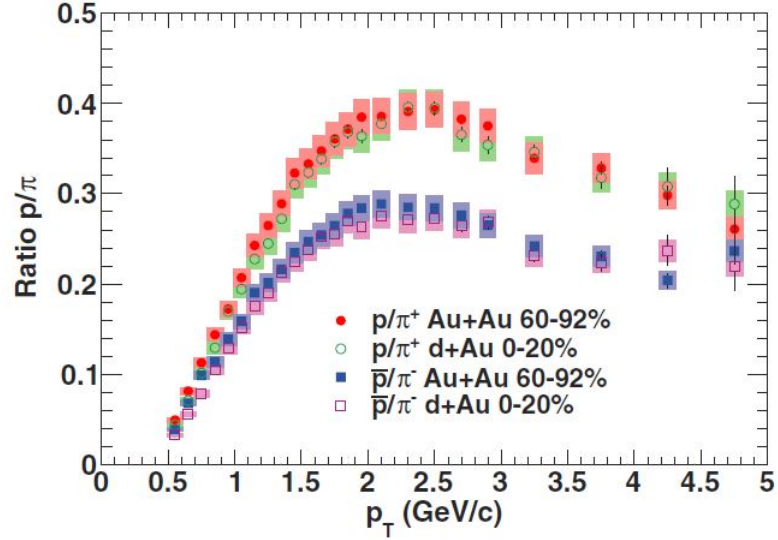


Figure 2.10: p/π ratios compared for central d+Au and peripheral Au+Au[4]

It may seem that the behavior of the two are contradicting since one is central and the other peripheral but we can see that the geometries of the collisions for the two cases are similar. The glancing peripheral Au+Au collisions create an "almond-like" QGP fireball whereas peripheral collisions in d+Au would behave such as a p+p collision since the number of participants is at a minimum when the collision is maximally peripheral. If we make the hypothesis that QGP formation is most likely with a higher number of participants then it follows that central d+Au collisions would be most likely to form a QGP. And so since physicists love reductionism and unification, and that the evidence makes one wonder if a QGP is formed in simpler systems, it would be advantageous to be able to describe the

two systems with a singular mechanism.

But are there even the building blocks to support such a notion that QGP is created in such a simple system as d+Au? Recombination is easy to justify in Au+Au since the large number of participants makes the formation of the QGP easily achieved and leaves a great abundance of free quarks that are able to recombine. What if we apply the same ideas to d+Au? Hwa and Yang asserted [27] that since hard scattering creates jets, jet formation generates a lot of soft outgoing partons. Furthermore, soft partons behave like an expanding QGP, that is to say, they behave like thermal partons. Thermal parton baryon enhancement is due to recombination. Since soft partons behave like thermal partons, could there recombination in d+Au, and if there is, could it be a sign that we should see other signs of QGP formation such as collective flow?

I postulate that there is sufficient evidence to say that the nuclear matter created

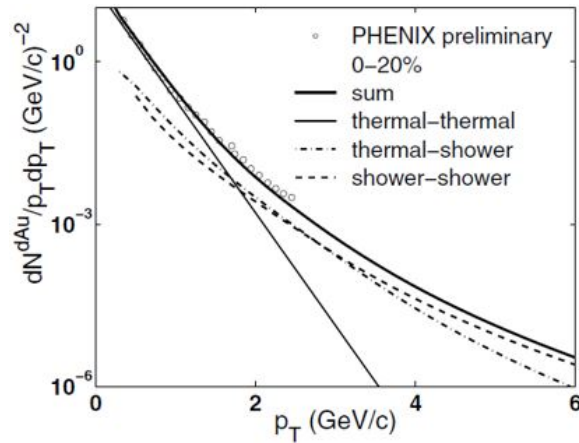


Figure 2.11: Pion transverse momentum distribution from d+Au collisions compared to one created with the recombination model

by d+Au behaves collectively and that there should be a non-zero elliptic flow measurement. Furthermore, this elliptic flow is dependent on particle species in that it exhibits baryon enhancement in the mid p_T range indicative of the formation of a QGP. Unknown phenomena of interest is the enhancement of strangeness. Recall that early fixed target experiments exhibited enhanced production of kaons compared to binary collisions, however there is no such enhancement in Au+Au collisions. Evidence of kaon flow or lack thereof could point to an interesting difference in the physics of the two different systems.

Chapter 3

Experimental Apparatus

3.1 The Relativistic Heavy Ion Collider

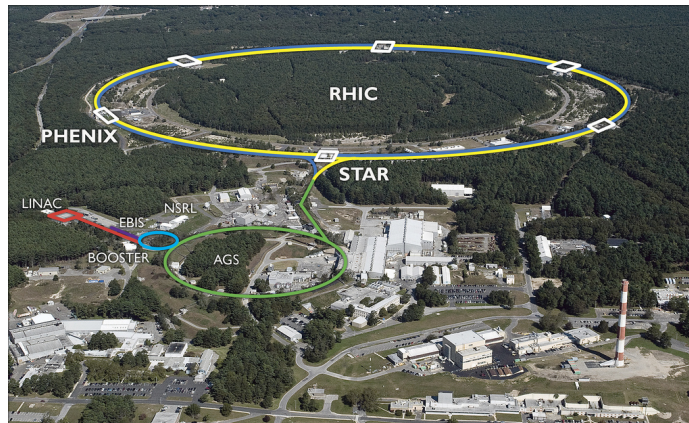


Figure 3.1: An Aerial view of BNL with RHIC and the AGS outlined and the locations of PHENIX and STAR mapped

Based at Brookhaven National Lab (BNL) on the east end of Long Island, New

York, the Relativistic Heavy Ion Collider (RHIC) is a particle accelerator and storage ring that is used to study the properties of nuclear matter, specifically the properties, formation of, and phase transition of nuclear matter into a novel state called the Quark Gluon Plasma (QGP). RHIC accelerates nuclei which are stripped of their electrons (heavy ions) to almost the speed of light and collides them together with enough energy to raise the system's temperature to that which is required to create the QGP.

3.2 From Start to Finish

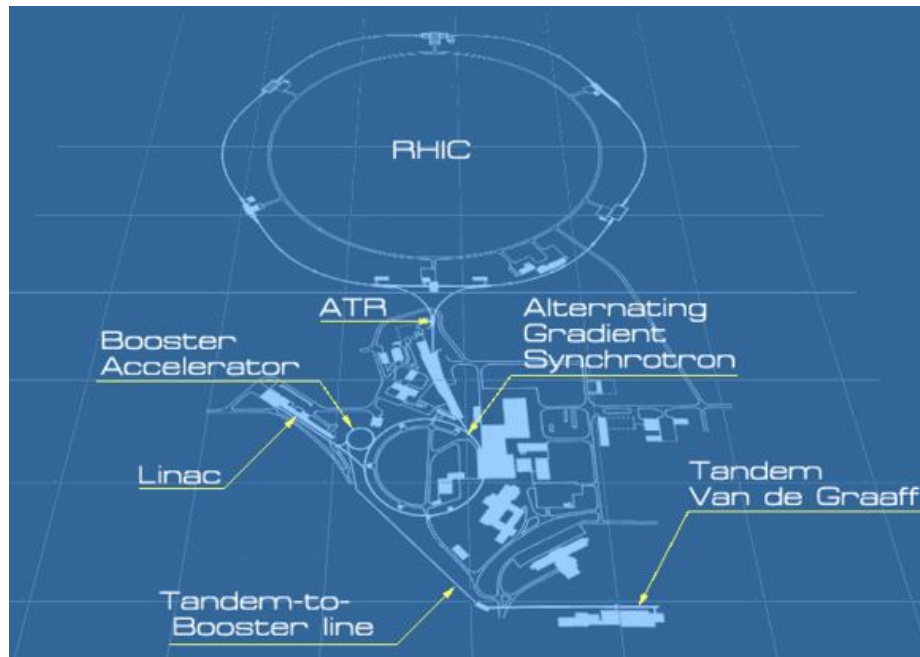


Figure 3.2: Illustration of all the smaller accelerators which are used together in order to boost ions to relativistic speeds at RHIC

The speeds achieved at RHIC is the result of many smaller accelerators working

in concert in order to boost the ions' speed faster and faster [10]. Ions begin their journey at a compact source and heavy ion accelerator called the Electron Beam Ion Source (EBIS) (located by the Linear Accelerator (LINAC) in figure 3.2). From there they are transferred to the a circular accelerator called the Booster Synchrotron which utilizes long-wavelength radio frequency electromagnetic waves allowing the ions to "surf" on their downward slope. The ions are then fed into the Alternating Gradient Synchrotron (AGS). No slouch in and of itself, the AGS was once the proverbial end-of-the-line where experiments took place and were studied and is responsible for three Nobel Prizes itself: the discovery of the muon neutrino in 1962, the discovery of charge-parity violation in 1963, and the joint discovery of the J/Ψ in 1976. The AGS uses the magnetic field gradients of 240 magnets, alternating them in order to boost the ions to 99.7% the speed of light after which it is transferred to the AGS-to-RHIC transfer line (AtR). The AtR is like a train switch yard wherein bunches of ions are fed into the RHIC rings. Bunches of ions are sent through either clockwise in one ring or counterclockwise in the other using a switching magnet.

RHIC is comprised of two concentric rings which are 3.8 kilometers in circumference. These rings use 1,740 helium cooled superconducting magnets to hold beams of these heavy ions which circulate in opposite directions within the two rings. Along the circumference of RHIC there are six points where the counter-circulating beams can be steered to collide (Interaction Regions or IR). Of these six IR, four have been used to house different detectors: the smaller, now defunct PHOBOS and BRAHMS experiments, and the larger still operational PHENIX and STAR experiments.

RHIC is an incredibly flexible machine capable of colliding various species of nuclei

from protons to Uranium [19] at a wide range of energies. Heavy ions such as Au can be accelerated as low as $3.85 \text{ GeV}/c^2$ and as high as $100 \text{ GeV}/c^2$ [32] with a combined center of mass energy of $200 \text{ GeV}/c^2$. When accelerating protons, RHIC is able to achieve up to $250 \text{ GeV}/u$ since the mass/charge ratio is smaller and is able to do so with polarized beams. It is also able to do this asymmetrically, that is to say, with two different species of nuclei, one in each ring. The system studied in this thesis is one such asymmetric system wherein a deuteron is collided with a gold ion with a center of mass energy of $200 \text{ GeV}/c^2$ (this system is referred to shorthand as "d+Au").

3.3 The PHENIX Detector

The analysis described in this thesis was made using the PHENIX detector which stands for: *Pioneering High Energy Nuclear Interaction eXperiment*. PHENIX is the largest of the experiments at RHIC and was designed specifically to study the QGP using a wide variety of particle probes at a very high rate with high accuracy.

It consists of a collection of various detectors assembled into four spectrometers called arms. The muon arms are used for studying physics phenomena at forward rapidity ($\eta = |1.1 - 2.4|$)[21] but the system of detectors used for the reconstruction of event tracks of import for this analysis are contained in the *Central Arm*.

3.3.1 Central Arm

Covering a rapidity range of $\eta = < |0.375|$, the central arm consists of an east and a west arm that cover the azimuth 90° each [12] and is a complex, multi-layered, multi-system

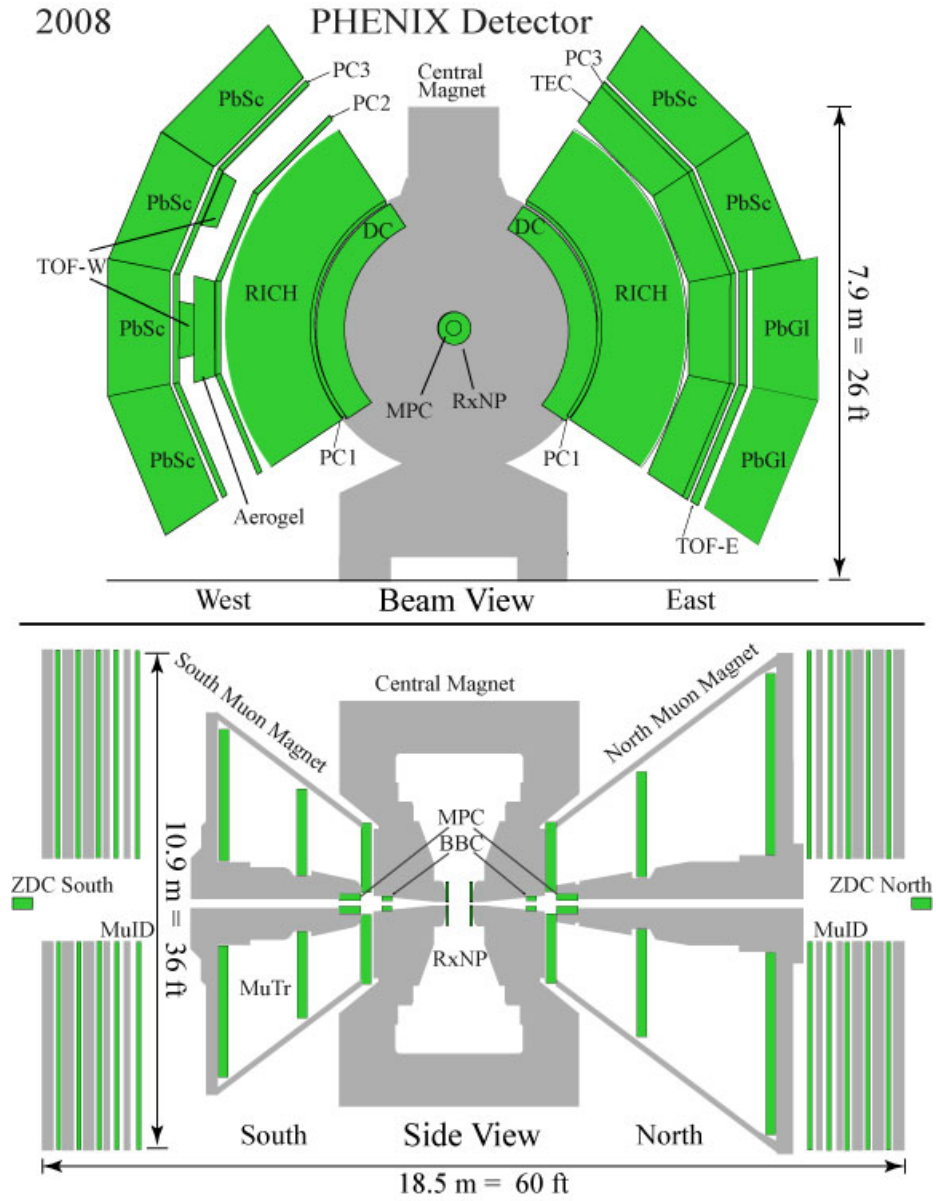


Figure 3.3: The configuration of the PHENIX detector for Run 8 (2008)

spectrometer capable of measuring a variety of particle probes. It is shown on the upper image labeled "Beam View" on figure 3.3 with individual subsystem detectors labeled. No single device is ideal for measuring every aspect of a collision event and as such, particle physicists design these complex detector systems such that different device technologies that are ideal for measuring specific quantities can all be used in concert to gather clean and precise data. Here I will discuss the various individual detectors in the central arm that I use in this analysis.

Drift and Pad Chambers

Particle trajectories are tracked using the Drift Chamber (DC) and the Pad Chambers (PC 1,2, and 3). The DC is a multiwire jet-type drift chamber with 12,800 readout channels. It is constructed from 6x80 wire nets in each arm. In principle the DC is similar to a wire chamber; When a charged particle travels through the gas in the DC the gas atoms are ionized and these ions and electrons are accelerated to anode wires which collect this ionization and sends a signal proportional to the ionization effect of the traveling particle. The DC is filled with a gas that is selected to have a uniform drift velocity close to the anode wires, i.e. a gas such that the traveling ions and electrons in the ionized gas have a linear relation in position and time such that $x(t) = v_{drift} * t$ within the active region [13], this gas is a mixture of equal parts Argon and Methane also chosen for the mixture's high gas gain amplification and low diffusion coefficient. In doing so and when combined with high accuracy timing calculation we are able to achieve a more accurate position and trajectory of outgoing particles. The wire nets in the DC are arranged in different predetermined ways with respect to the beam axis. The six nets are designated names: X1, U1,

V1, X2, U2, and V2. The X wires are configured to be parallel to the beam axis and the U and V wires are tilted by an angle of 4.5° . This angular bias allows the DC to measure the track's z-component with high resolution and the multiple radial layers of wire are used to measure track curvature to determine momentum. The DC is the first detector subsystem that outgoing particles created in a collision pass through and is used in conjunction with other detectors in order to accurately determine track trajectory through all of the detectors in the central arm.

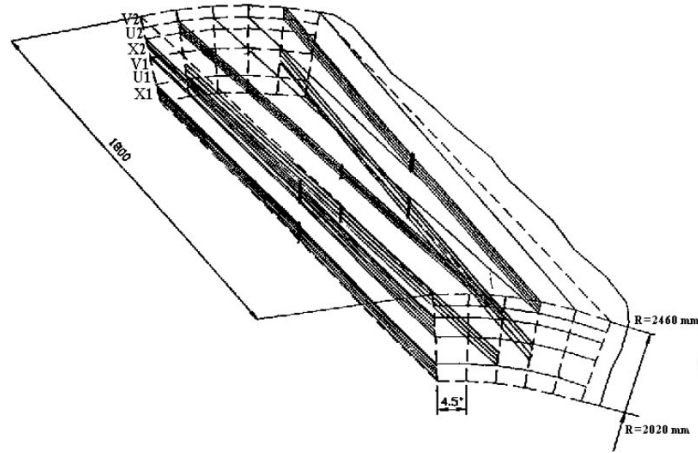


Figure 3.4: A diagram showing the configuration of the wire nets in the DC

The Pad Chambers are three individual layers of pixel detectors. These pixels are arranged in 9 pixel clusters called "pads" that are readout by a single channel [35]. The pads in the closest-to-collision PC (PC1) are 8.4 mm x 8.45 mm and the pads in PC2 and PC3 are sized to maintain the same angular resolution at farther radial distances. The PC and DC have the same azimuthal coverage as the rest of the central arm and are located

at increasing concentric distances from the collision vertex, the DC being the inner most detector, followed immediately by PC1. PC2 only exists in the west arm however PC3 exists in both arms. The small size of the individual pads allows for a large pixel density important for maintaining the separation of individual track signals in a high luminosity, high multiplicity event such as that of central heavy ion collisions. Since we can use these detectors to accurately determine particle track trajectories, and since charged particles under the influence of a magnetic field curve, the determined curvature can be used to determine track momentum. This track location data is also used to match with other detector data such as calorimetry, time of flight, and Cherenkov counters.

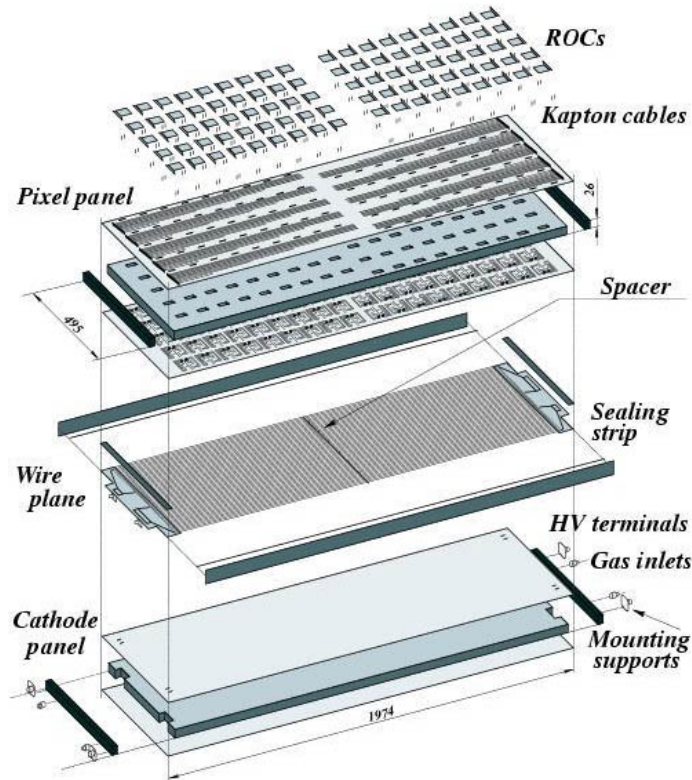


Figure 3.5: A blown up schematic showing the anatomy of the Pad Chambers.

TOF: Time Of Flight Detectors

In addition to the track matching detectors this analysis utilizes the Time of Flight (TOF) detectors which are high accuracy timing detectors that measure the time it takes for charged particles traveling through the central arm to go from the event vertex to the detector[33]. There are two TOF detectors in PHENIX, one on the east DC arm and one on the west arm. Located 5 meters away from the collision vertex and in the lower two sectors of the east arm, the TOF East (TOFE) is a scintillation detector with a timing resolution

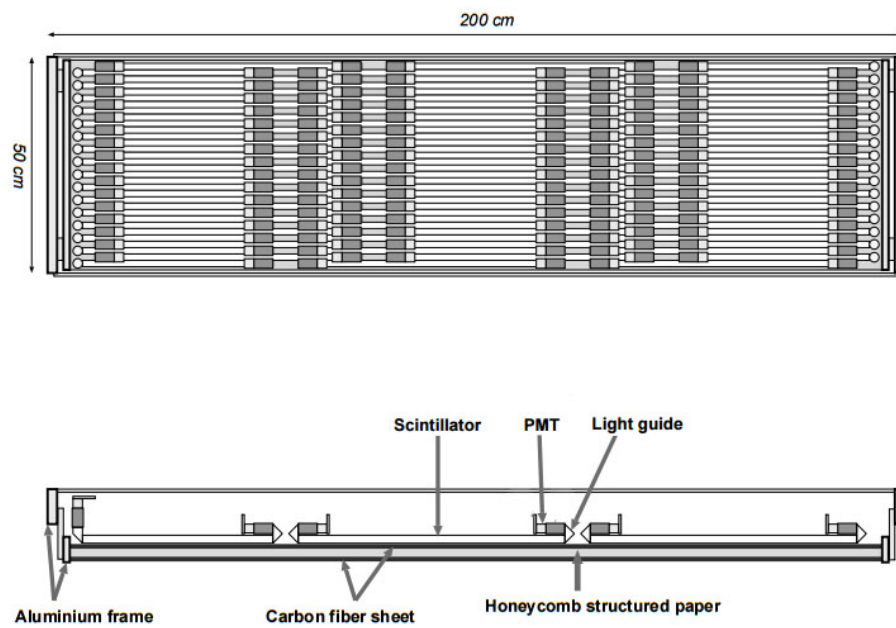


Figure 3.6: A schematic of the slat layout in the TOFE

of $\Delta t_{res} \sim 80ps$. It covers $\Delta\phi = \pi/4$ and $\eta < |0.35|$.

Scintillators are a special type of material that fluoresces when it absorbs radiation. The TOFE is comprised of 1000 "slats" of plastic scintillation material with two photomultiplier tubes (PMT) on either end of the slats which amplify the fluorescing photons caused by charged particles that pass through the scintillators. Since we know the length of the slat and the speed of light in the scintillation material we can easily calculate both the time when the particle first hit the slat (T_0) and the position where the particle hit the slat (y).

$$T_0 = \frac{(T_1 + T_2) - L/v}{2}, \quad y = \frac{T_1 - T_2}{2}v \quad (3.1)$$

Where T_1 and T_2 are the times measured by PMTs 1 and 2 respectively, L is the length of the slat, and v is the speed of light in the scintillator.

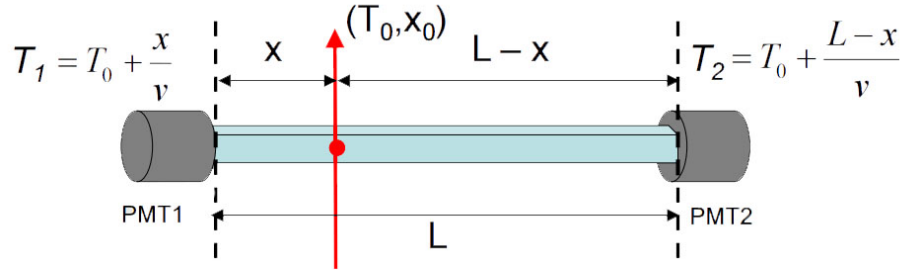


Figure 3.7: An illustration of a single slat in the TOFE

In the west arm, the TOF West (TOFW) is a 1024 channel Multi-gap Resistive Plate Chamber (MRPC) detector with a timing resolution of $\Delta t_{res} < 100ps$, located 4.85 m from the collision vertex and also covering $\Delta\phi = \pi/4$ and $\eta < |0.35|$. The MRPC works

on the same principle as a basic Resistive Plate Chamber which is comprised of two high resistivity plastic (bakelite) plates separated by a volume of gas. On one resistive plate is a sheet of conducting material which is used to maintain a constant electric field across the gas gap. The other resistive plate has an array of conducting readout strips. When a charged particle travels through the gas it causes an electron avalanche similar to what happens in a drift chamber. This electron avalanche is accelerated under the influence of an externally applied electric field toward one of the readout strips resulting in a "hit" signal which is then amplified by electronics.

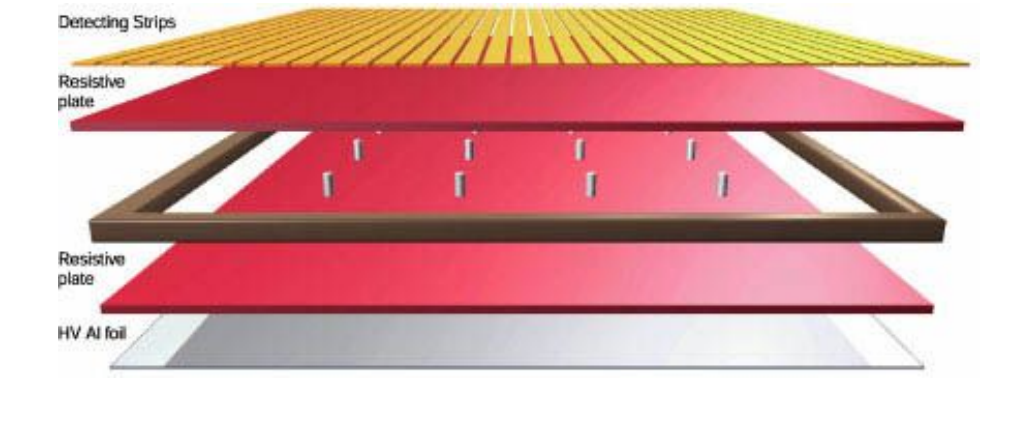


Figure 3.8: Diagram of a basic RPC [38]

A MRPC is a version of an RPC with alternating layers of the resistive material and gas gaps sandwiched together with the high voltage surface and readout strips on the outermost sides of the device [6]. The resistive plates inside the sandwich are electrically isolated and are transparent to the fast signals of incoming particles. Initially the externally applied electric field induces charges on the surfaces of the resistive plates causing each of the small gas gaps to be held at the same potential, and since each incoming particle ionizes

the gas and deposits the same amount of one charge on one side of the plate and the opposite charge on the other, the potential in each individual gap is held constant. This means that the total signal the strips see is the *sum* of all of the electrical activity in each of small gaps. By using this configuration a greater precision is allowed than conventional RPC designs and lends itself well to high precision timing detectors.

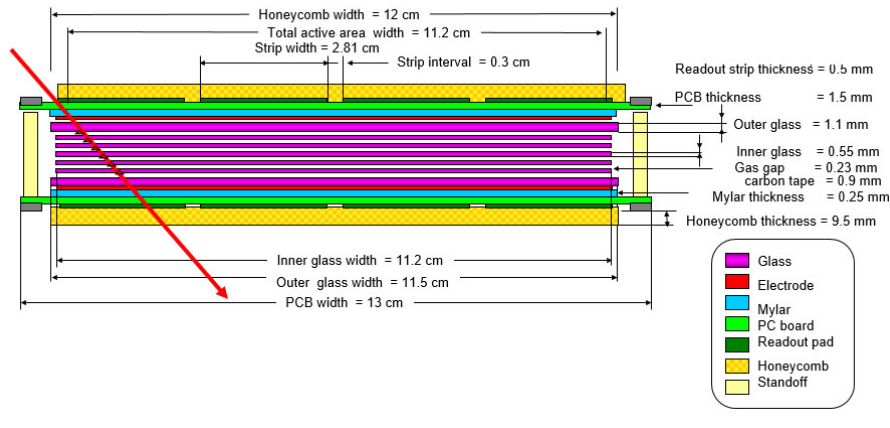


Figure 3.9: Cross sectional diagram of the MRPCs used in the TOFW

ACC: Aerogel Cherenkov Counter

As track momentum increases the signal width of the particle masses increases. The high resolution capabilities of the TOF detectors only allows them to be able to separate π^\pm , k^\pm , and p / \bar{p} signals up to certain transverse momentum p_T thresholds. The distinct masses of the particles of interest do provide an additional method of separating particle signals since if you were to give two particles of different mass the same momentum they would have distinct velocities. This is the principle with which a Cherenkov detector works.

Cherenkov radiation is light that is emitted in a material when a charged particle travels through it with a velocity faster than the speed of light in that medium. This medium called a Cherenkov radiator can be carefully selected such that its intrinsic speed of light is such that lighter particles with higher velocities cause Cherenkov radiation but heavier particles which travel slower given the same momentum will not. Using this, a Cherenkov detector acts as a logic detector categorizing tracks as those that either "fire" or "veto", that is to say tracks that radiate versus tracks that don't. In the case of separating π^\pm mesons from k^\pm mesons for p_T tracks where their mass signals overlap so strongly that they cannot be uncorrelated, the radiator was chosen such that the pions will fire the detector and the kaons will not. Pions and kaons are indistinguishable for $p_T > 2.8$ GeV/c, so the radiator chosen to separate the signals is a silica aerogel ($n \approx 1.011$).

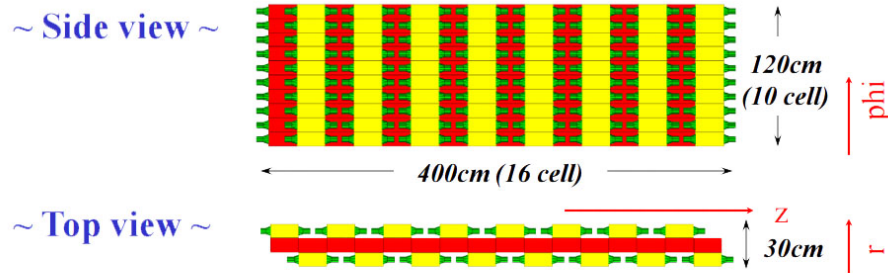


Figure 3.10: A schematic of the Aerogel Cherenkov Counter

The Aerogel Cherenkov Counter (ACC) is comprised of 160 tiles of silica aerogel. Each tile is affixed to an integration cube which allows for radiated cherenkov photons to reflect internally until they hit a PMT. Each integration cube is filled with air and is covered

on all exposed sides by a goretex reflector except for the "front" facing aerogel tile side and the two cutouts where the PMTs attach. There are two PMTs located opposite from each other for each cube. To account for the space taken by PMTs on the ends of the tiles the ACC is two sided and the tiles are oriented such that the opposite side tile occupies the gap where PMTs would be situated. There are 10 rows of 8 tiles on each side for a total of 160 tiles.

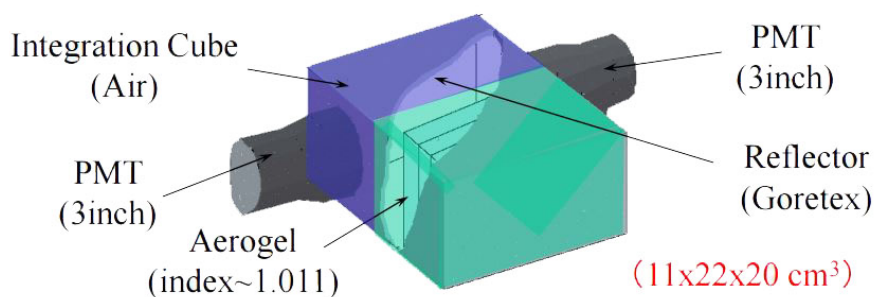


Figure 3.11: A schematic of one tile in the ACC

The ACC is located in the west arm covering the half of the azimuthal coverage that the TOFW covers and with the same rapidity coverage. When used in conjunction with the TOFW it can provide pion/kaon separation for $p_T < 4$ GeV/c and can discriminate protons for $p_T < 7$ GeV/c. The total capabilities of the combination of the TOFW + ACC is shown in the following chart.

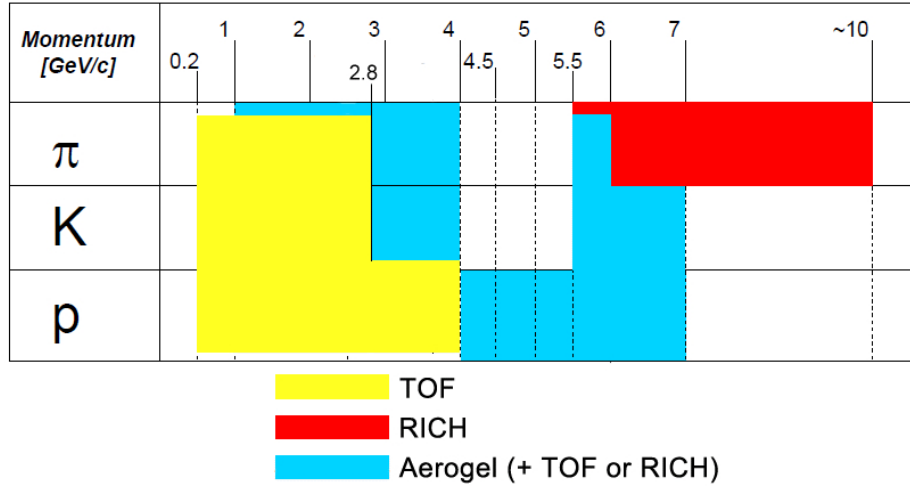


Figure 3.12: Chart of Particle Identification capabilities over a range of transverse momentum

EMCal and RICH: Electromagnetic Calorimeter and Ring Imaging Cherenkov Counter

Two other detectors that provide important track data are the *Electromagnetic Calorimeter* (EMCal) and the *Ring Imaging Cherenkov Counter* (RICH). Each arm has full coverage with both the RICH and the EMCal and they are often used together in order to study electrons via the EMCal/RICH Trigger (ERT).

As evident from it's name, the RICH is a Cherenkov counter that is used in a similar fashion as the ACC: to discriminate between particle species using Cherenkov radiation as a logic trigger. In the case of RICH, we are interested in separating pion and electron signals. It is filled with CO_2 which was chosen because it would allow electrons to radiate at very low p_T ($> 0.018 \text{ GeV/c}$) while pions will not until the relatively high p_T

of 4.87 GeV/c. Cherenkov radiated photons are emitted parallel to each other along the track path as electrons move through the detector. The outer surface of the RICH is a series of mirrors arranged to form a spherical mirror which focusses that Cherenkov light onto the 2560 PMTs/arm which line the inner surface of the RICH. This results in a ring shaped Cherenkov signature as measured by the PMTs, hence the name: Ring Imaging Cherenkov Counter.

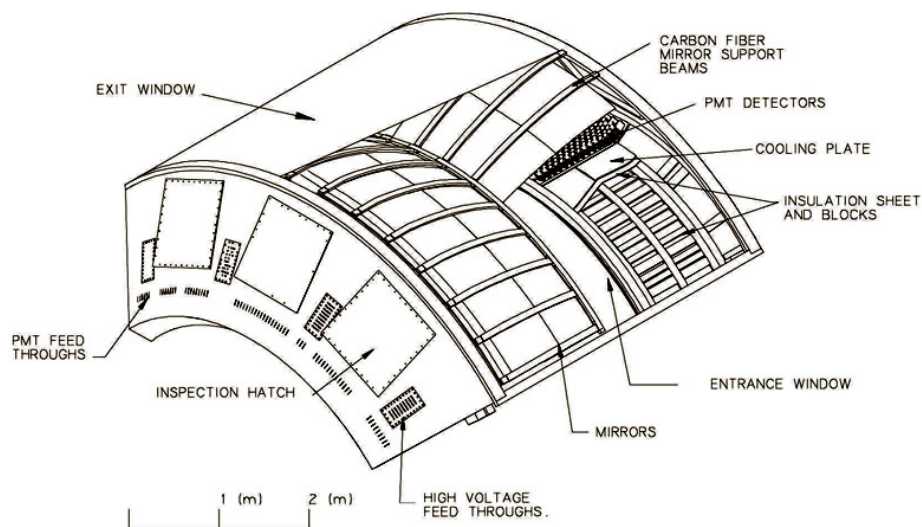


Figure 3.13: A diagram of the RICH

The EMCal provides an energy measurement for charged tracks and is broken up into eight sectors, four sectors in each arm [12]. Six of the sectors (all four of the west arm and the top two in the east arm) are made of channels comprised of alternating layers of lead and scintillator (PbSc) material. The lead layers cause incoming particles to shower into the scintillator layers which generate light that is detected by PMTs. The lower two sectors in the east arm are comprised of 10,080 uniform lead glass Cherenkov radiator towers (PbGl).

These towers have PMTs attached on one end and are wrapped individually in reflective mylar and shrink wrapped to form *modules*. They are then placed in grid-like networks and each 16 module x 12 module structure is read out by one photodiode/preamplifier combination.

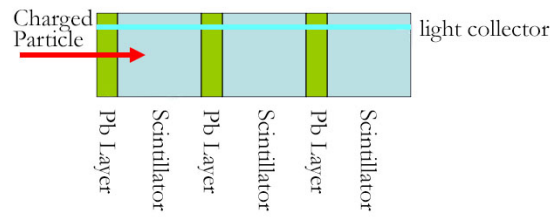
Though it may seem odd to have two types of detectors in the EMCal, there is a method to the madness. Both have their own strengths, PbSc is more linear in response and is better at timing than PbGl thanks to its alternating layers, whereas PbGl is a tried and true design used in previous experiments such as WA98 at the SPS at CERN for it's exceptional granularity and accurate energy measurement. Because they are two separate systems, they have different systematics and therefore we have a higher confidence level for the physics results from the EMCal.

3.3.2 Forward and Global Detectors

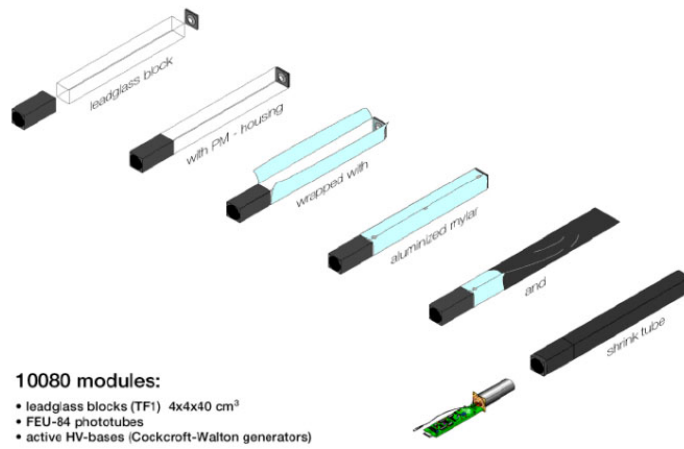
Though the bulk of this analysis is dependent on the central arm detectors, many aspects of reconstruction, namely event characterization (start of the event timer, the event vertex, centrality, and event reaction plane) is dependent on a handful of forward detectors which I will briefly discuss here.

BBC: Beam-Beam Counter

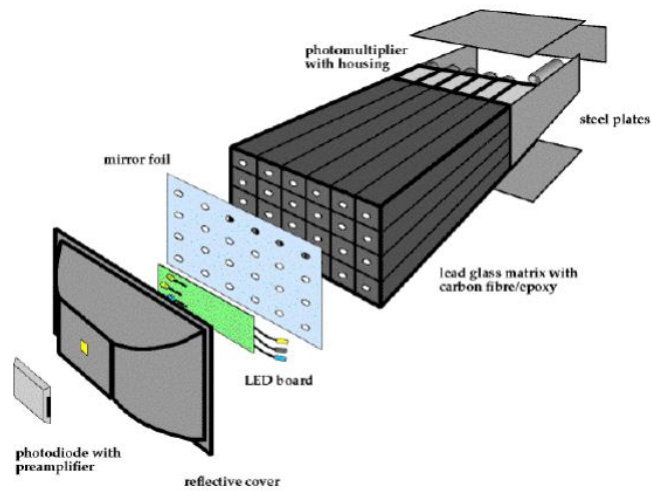
Of the forward detectors, the *Beam-Beam Counter* (BBC) is probably the most important because of its ability to measure the various global event parameters. There are two BBCs, one on the north side and one on the south side of PHENIX both equidistant



(a) Schematic of PbSc module.

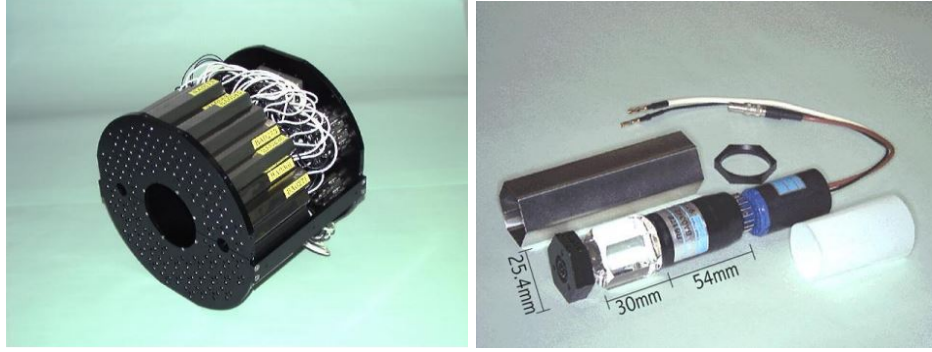


(b) Construction of PbGl modules.



(c) One PbGl super module

Figure 3.14: Schematics of EMCal components



(a) An illustration of a BBC

(b) A single element of the BBC

Figure 3.15: The Beam Beam Counter

from the center of the interaction region (IR). The constituent detector elements are made of quartz Cherenkov radiators attached to meshed dynode PMTs housed in hexagonal encasement. These elements are arranged in a toroidal shape in order to allow the ion beams to pass through the center while still getting full 2π azimuthal coverage. The BBCs cover $3.1 \leq \Delta\eta \leq 4$ in pseudorapidity.

ZDC/SMD: Zero Degree Calorimeter and Shower Max Detectors

Crucial to the determination of event centrality is the ability to count the number of spectator particles. Since neutrons have no charge we can place a calorimeter at high rapidity behind an IR dipole magnet which we can use to "sweep" away charged particles like proton spectators and other charged track noise. The *Zero Degree Calorimeter*[14] is comprised of a ribbon of acrylic fiber optic strands sandwiched between two tungsten plates. The tungsten plates act as a dense absorber for the neutrons to hit and shower into resulting in detectable photon yield in the fiber optic ribbon. Sandwiched between

modules of the ZDC is a hodoscope called the *Shower Max Detector* (SMD). The SMD is comprised of 21 0.5 cm x 0.5 cm scintillators and is used to measure the centroid of the shower in cartesian coordinates since the ZDC only measures energy[40]. The ZDC is used in conjunction with the BBC in order to determine centrality. Since more peripheral collisions mean more spectators and therefore more neutrons to hit the ZDC, the higher the energy measured by the ZDC the more peripheral the event (see fig 3.16[22]).

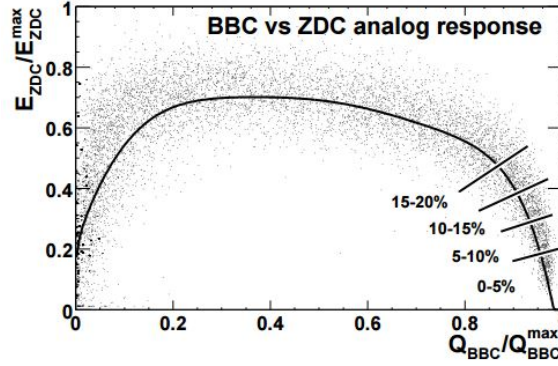


Figure 3.16: Centrality bins as determined by ZDC energy versus BBC charge sum[22]

MPC: Muon Piston Calorimeter

The *Muon Piston Calorimeter* (MPC) was a needed upgrade to PHENIX that provided calorimetry at very high rapidity[30]. It was installed in two parts: first in the south in 2005, then in the north in 2006 and was commissioned to reconstruct π^0 and η mesons for various forward physics analyses. Nestled in a gap in the piston of the Muon Magnet Arms, it provides full azimuthal coverage at $3.1 \leq |\eta| \leq 3.7$ (3.9 in the north) and is comprised of 196 (220 in the north) Lead Tungstate $PbWO_4$ crystal scintillator towers

attached to avalanche photodiodes with preamplifiers to measure the electromagnetic shower photons. For this analysis, the MPC is used as a another measurement point for determining the reaction plane resolution correction.

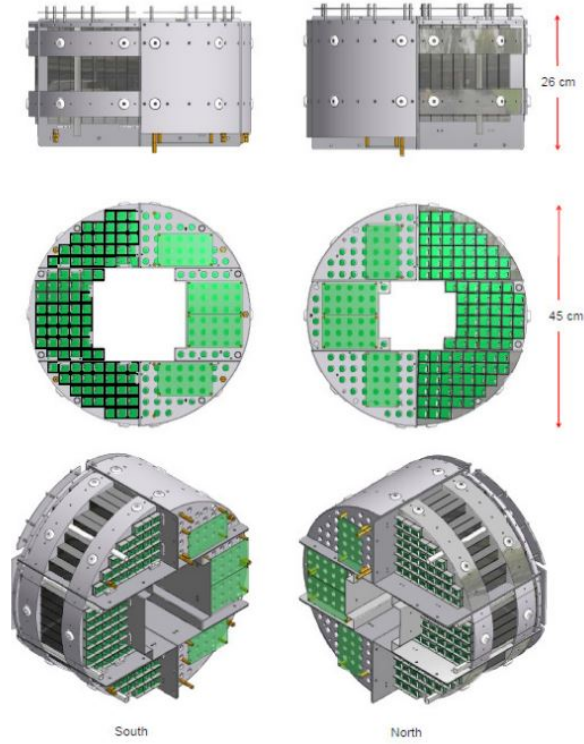


Figure 3.17: Schematic of the MPC

RXNP: Reaction Plane Detector

Chapter 4

Heavy Ion Collisions: A Primer

4.1 Measurable Quantities

Due to the complexity inherent in colliding large nuclei containing a large number of nucleons (for instance 197 nucleons in Au) there is a multitude of metrics we can use to quantify the collision and the evolution of what happens after. For clarification, when talking about high energy physics analyses we refer to all data gathered from a single collision of two nucleons as an *event*. The location where the collision takes place is called the *event vertex* or often in collaboration literature since the z-axis is along the beam axis, the *z vertex*. The high luminosity of heavy ion collisions (437 nb^{-1} in 9 weeks for the data used in this analysis: Run 8 d+Au), produces a plethora of particles. As these particles travel from the event vertex through the various layers of detectors under the influence of the PHENIX magnetic field it leaves its own signature on each detector it passes through. These signatures for each given particle can be matched to form a trajectory from the event vertex through PHENIX. The set of data corresponding to location, kinematic, and detector

specific variables (i.e. charge deposited, clusters fired, Cherenkov photons, etc) is called a *track*. The determination of these variables is the topic of this chapter.

4.2 Event Characterization

When describing a heavy ion collision it is useful to introduce quantities that describe the initial conditions of the interacting nucleons. The set of variables that correspond to these conditions are called the *event* or *global* variables. They are used to accurately locate where the event took place inside the detector and the geometric configuration of the nuclei at the time of collision. These event variables are reconstructed largely by the extremely forward detectors: the *Beam-Beam Counters* (BBC) and the *Zero Degree Calorimeters*.

4.2.1 Centrality

One such variable is *centrality* and is used to describe how "head-on" two ions collide, that is, do they collide with complete cross sectional overlap or do they just barely glance each other. It is useful to quantify this overlap with a quantity called the *impact parameter*, \mathbf{b} . We define this impact parameter by measuring the distance between ion centers as depicted on the left-hand side of figure 4.1. Note that the ions in this illustration appear squished in the x axis due to Lorentz contraction. Therefore, small impact parameters correspond to large ion-ion overlap in the collision and large impact parameters refer to glancing collisions. In heavy ion physics we call collisions with small impact parameters *central collisions* and those with large impact parameters *peripheral collisions*.

Experimentally it is impossible to measure the distance between the two ion centers. In practice, centrality can also be quantified by the number of *participants*, or the number of nucleons that collide/interact with each other, versus the number of *spectators*, or the number of nucleons that do not collide. Since we know the number of total nucleons in each ion we can determine the number of participants by counting the number of spectators and subtracting them from the total number of nucleons. Colliding nucleons will produce particles in all directions however spectating nucleons will continue to travel down the beam pipe. We therefore can count the number of spectators by placing detectors at very high rapidity.

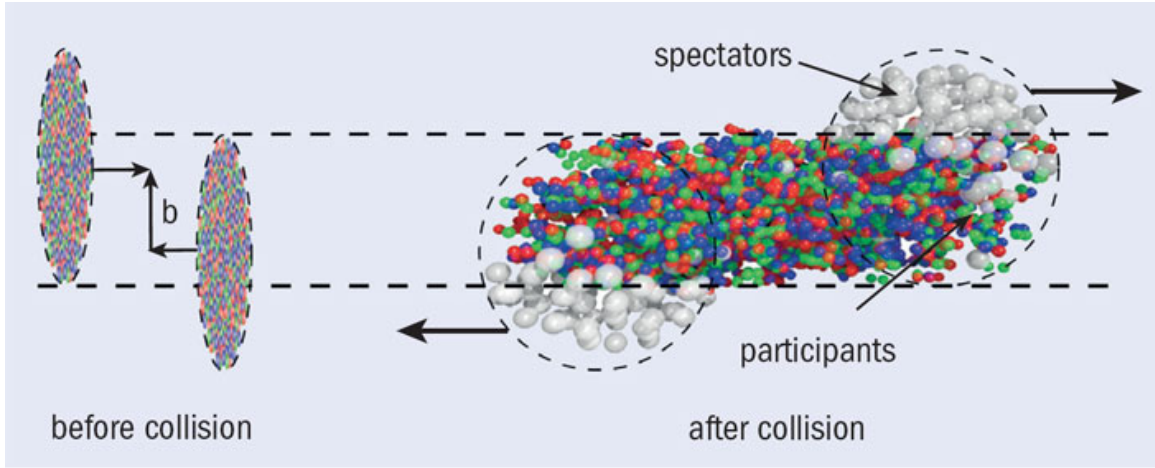


Figure 4.1: Spectators and participant nucleons in a heavy ion collision [39]

Extending the terminology from impact parameters, we then define a collision with a large number of participants to be a *central* collision and a collision with a small number of participants: a *peripheral* collision. These are quantified in percents, 0% being

most central collisions i.e. highest number of participants, $b = 0$, two colliding ions overlap completely, and 100%: ions completely miss each other, i.e. there are no participants, $b > R_{nucleus}$. Since ions are spherical in shape, centrality can be used as a way of describing the geometry of the collision region, central collisions have a more circular shape whereas peripheral collisions have a more almond-like shape.

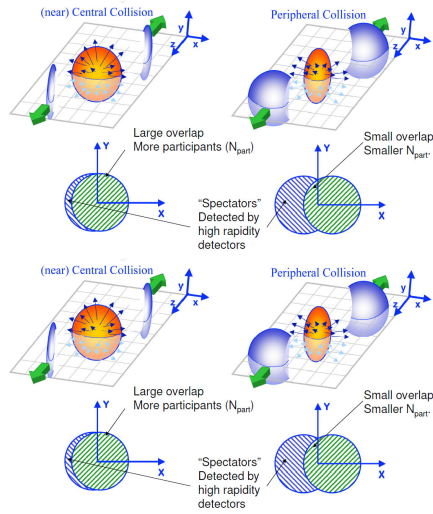


Figure 4.2: Spectators and participant nucleons in a heavy ion collisions.

4.2.2 Event Vertex and Timing

The event vertex is the location along the beam axis where the collision happened relative to the equidistant point between the two beam beam counters. That is, an event vertex value of 0 would be exactly in the center of the PHENIX detector, at equal distance from both BBCs. When a collision happens, the non colliding nucleons (spectators) continue to travel through the interaction region and are detected on the other side by the two BBCs.

The time at which each cluster of spectators hits an individual BBC is measured. These two times, T_1 and T_2 respectively, can be used to calculate both the event vertex (z_{vtx}) and the initial time the collision takes place (T_0) as follows[34]:

$$z_{vtx} = \frac{T_1 - T_2}{2c} \quad \text{and} \quad T_0 = \frac{T_1 + T_2}{2} \quad (4.1)$$

This initial time is used to start the stopwatch of the event and is used in conjunction with other detectors to find the time a produced particle takes to travel from the vertex to a detector.

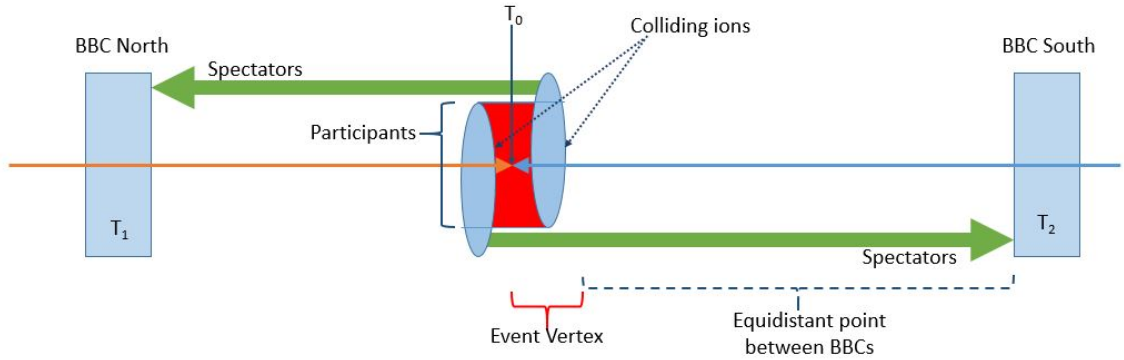


Figure 4.3: Diagram of BBC event characterization

4.3 Track Reconstruction

4.3.1 Variables for Track Selection

After the collision, particles fly outward from the vertex under the various mechanisms that take place within the formation and evolution of the QGP. Due to the high multiplicity of tracks resulting from a heavy ion collision and the various complexities that arise when using a multifaceted complicated detector system to reconstruct track trajectories, it is important to quantify the quality of the tracks to discern which tracks are able to be reconstructed cleanly versus those which, for whatever anomalous reasons, would not be advantageous to analyze.

The process of determining the track trajectory through the PHENIX detector is called *track matching* and it utilizes the various layers of the Drift Chamber and Pad Chambers in concert to determine track momentum due to the varying curvature of tracks of different momenta traveling through a magnetic field. track quality

4.3.2 Particle Identification

Using the TOF detectors' high resolution timing measurements I am able to identify particles which have long lifetime relative to the event duration i.e. particles whose lifetimes are long enough such that they do not decay before leaving the detector. For this analysis, these particles of interest are the charged pions (π^\pm), charged kaons (k^\pm), and protons/antiprotons (p/\bar{p}). Since the masses of these particles are distinct, plotting the momentum vs time of flight can show clear separation between pion, kaon, and proton signals (see fig 4.4).

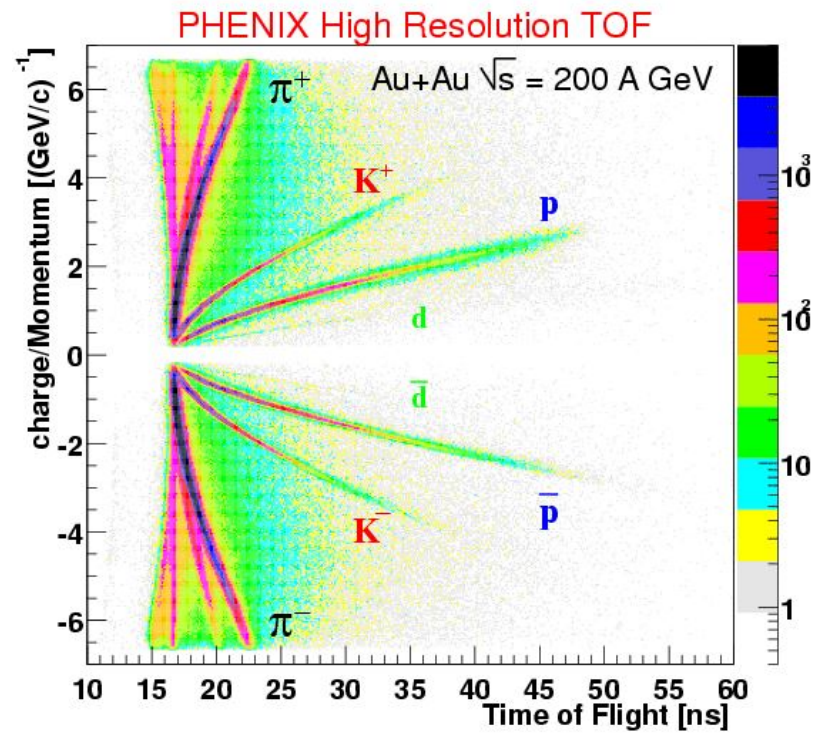


Figure 4.4: Particle separation in the TOF [29]

While visually the individual particle signatures are easily identifiable, computationally it is advantageous to convert units so that the signatures only depend on a single variable. After the collision, the QGP fireball is expanding rapidly however the constituent outgoing tracks traversing the distance scales in the detector do not experience appreciable deceleration. We know from basic kinematics that we can calculate the velocity, v , of an object traveling at a constant speed:

$$v = \frac{L}{t} \implies t = \frac{L}{v}, \quad (4.2)$$

where t is the time it takes to travel some path length, L . It is useful to define the relative speed of the particle compared to the speed of light, c , as $\beta = v/c$ and substitute it in for v . We also know from the relativistic identities that $\beta = p/E$ and $E^2 = p^2 + m^2$. The equation is then:

$$t = \frac{L}{v} = t = \frac{L}{c\beta} = \frac{L}{c} \frac{E}{p} = \frac{L}{c} \frac{\sqrt{p^2 + m^2}}{p}. \quad (4.3)$$

which can be solved for m^2 to give the mass vs time relation:

$$m^2 = p^2 \left\{ \frac{t^2}{L^2} - 1 \right\}. \quad (4.4)$$

Note that since the distance from the event vertex to the detector is constant and for that distance scale the velocity, and therefore also the momentum, can be treated as constant, m^2 depends on two constant terms if we take measurements in bins of p . Since we are talking about radially outward traveling tracks, this p is, in practice, p_T . Therefore if we do arithmetic on the track variables we are able to plot m^2 vs p_T which gives us a

much easier to analyze representation of the individual particle signatures.

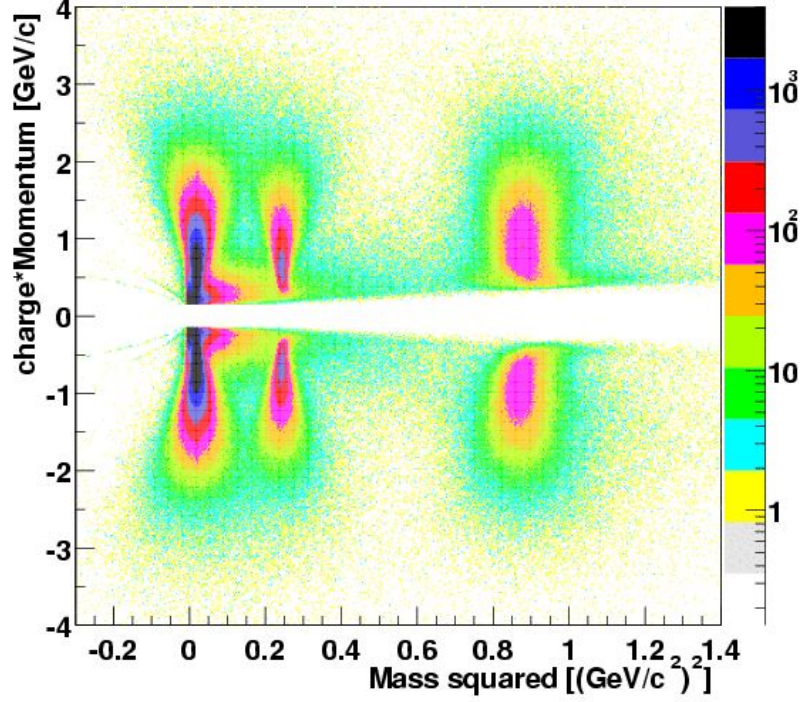


Figure 4.5: m^2 vs p_T showing clear constant separation of particle signatures. [29]

4.4 Nuclear Modification Factor

Since heavy ion systems are comprised of many nucleons colliding, one way we differentiate between phenomena from singular nucleon-nucleon collisions and phenomena created from interactions of nuclear matter it is convenient to define a quantity that describes how different a system of N colliding nucleons differs from a system of two colliding nucleons scaled up by N , often referred to as *Binary Scaling*. This quantity is called a

Nuclear Modification Factor and is usually denoted with the letter R and two subscripts defining what kind of Nuclear Modification Factor it is:

$$R_{AA}(p_T) = \frac{1}{\langle N_{coll} \rangle} \frac{dN_{AA}/dp_T}{d\sigma_{pp}/dp_T}, \quad (4.5)$$

where dN_{AA}/dp_T is the differential yield in the system, $d\sigma_{pp}/dp_T$ is the differential cross section in proton-proton collisions, and $\langle N_{coll} \rangle$ is the number of binary collisions. Given this definition if $R_{AA} = 1$ then we expect no new phenomena in the system, that is, the system comprised of N colliding nucleons behaves exactly as we'd expect N proton-proton collisions to behave. If $R_{AA} > 1$ it is said that interactions with the nuclear material enhances production and vice versa with $R_{AA} < 1$, production is suppressed.

Chapter 5

Anisotropic Flow

In the moments immediately after a collision event, the outwardly expanding behavior of the newly formed QGP can be studied to better understand the QCD processes that take place both during formation as well what happens as this QGP dissipates. Though it expands in all directions it is the expansion about the azimuth that best describes the behavior of this fluid. Often physicists like to describe the behavior of phenomena using a series expansion of orthogonal functions. Since the azimuthal angle runs from 0 to 2π , this azimuthal expansion can be treated as a harmonic function which lends itself well to parameterization using a Fourier series. Recall that a Fourier series can approximate a function $f(x)$:

$$f(x) = \sum_{n=-\infty}^{\infty} A_n e^{i(2\pi nx/L)} \quad (5.1)$$

where

$$A_n = \frac{1}{L} \int_0^L f(x) e^{-i(2\pi nx/L)} dx \quad (5.2)$$

are said to be the Fourier **coefficients** or often, since they approximate harmonic functions, Fourier **harmonics**. It is a tautology that the exponential term can be written as the sum of a real cosine term and an imaginary sine term:

$$f(x) = \sum_{n=1}^{\infty} A_n \cos(2\pi nx/L) + i \sum_{n=1}^{\infty} B_n \sin(2\pi nx/L) \quad (5.3)$$

where

$$A_n = \frac{1}{L} \int_0^L f(x) \cos(2\pi nx/L) dx \quad (5.4)$$

and

$$B_n = \frac{1}{L} \int_0^L f(x) \sin(2\pi nx/L) dx \quad (5.5)$$

Since we define $\phi = 0$ to be along the waist of the ellipsoidal shaped QGP and not at the poles, odd function contributions (sine terms, B_n) to the Fourier series can all be ignored. Therefore if we wish to approximate the shape of the outgoing flow from the QGP we can define the rate of change of outgoing particle tracks vs transverse momentum and approximate it with a Fourier series. Flow anisotropy of the QGP can then be written as:

$$E \frac{d^3 N}{dp^3} = \frac{1}{2\pi} \frac{d^2 N}{p_T dp_T dy} \left(1 + \sum_{n=1}^{\infty} 2v_n \cos(n(\phi - \Psi_r)) \right), \quad (5.6)$$

where:

$$v_n = \left\langle \cos(n[\phi - \Psi_{RP}]) \right\rangle \quad (5.7)$$

are the n-th order Fourier coefficients that describe the azimuthal shape of the QGP's outward expansion and ϕ is the azimuthal angle with respect to the reaction plane. Each n-th order coefficient scales the amount of expansion that behaves like $\cos nx$.

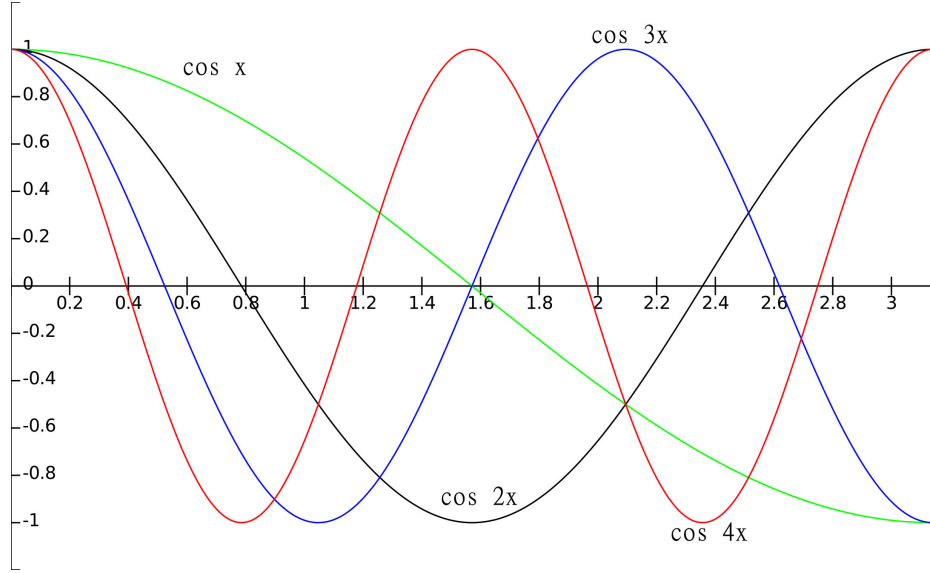


Figure 5.1: Plots of the first four harmonics of a cosine series

From studying the behavior of these various harmonics we can see that for $n = 1$, $\cos x$ is a maximum at $\phi = 0$ and a minimum at $\phi = \pi$ which would correspond to a preferential flow in the $\phi = 0$ direction. Therefore the $n = 1$ flow coefficient is often called *directed flow*. For the case of $n = 2$ we see that again there is a maximum at $\phi = 0$ and again at $\phi = \pi$ which corresponds to maximal flow at the waist of the ellipsoidal QGP. This expansion about the waist of the collision region results in an elliptical preferential flow, a term which is shortened to *elliptic flow*. There are higher order harmonics which can describe various other phenomena of QGP flow which are beyond the scope of this analysis.

Chapter 6

Event Plane

6.1 Determination of Event Plane

6.2 Event Plane "Flattening"

6.3 Event Plane Resolution Correction

The method used for this analysis is called the *Three Subevent Method* and can be calculated by comparing the event plane measured with one detector to measurements made by two other detectors.

$$Res\{2k\Psi^A\} = \sqrt{\frac{\langle\cos(2k[\Psi^A\Psi^B])\rangle\langle\cos(2k[\Psi^A\Psi^C])\rangle}{\langle\cos(2k[\Psi^B\Psi^C])\rangle}} \quad (6.1)$$

Chapter 7

Results

7.1 Charged Track v_2

7.2 Separating Particle Signals

7.2.1 Single Gaussians

7.2.2 Gaussian Mixing

7.2.3 ACC as a Pion Discriminator

7.3 Yield vs Event Plane

7.4 Identified Particle v_2

Chapter 8

Error Analysis

8.1 Systematic Errors

Chapter 9

Summary and Conclusions

9.1 Discussion

9.2 Conclusions

Appendix A

PHENIX Coordinate System

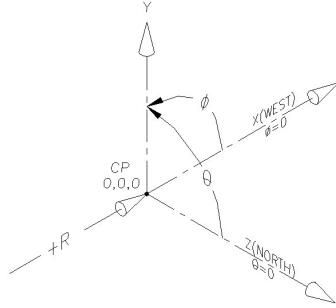


Figure A.1: PHENIX coordinate system

The PHENIX coordinate system in Cartesian coordinates is defines the beam line as the z-axis with the north side of the detector being the positive going direction, due west being the positive going x-axis, and straight up being the positive going y-axis. For spherical coordinates, the azimuthal angle ϕ spans 2π about the z axis with $\phi = 0$ pointing due west, i.e. along the x-axis. The polar angle θ is often converted to pseudorapidity for

analysis. Pseudorapidity, often shortened to "rapidity," is defined as:

$$\eta = -\ln \left[\tan \left(\frac{\theta}{2} \right) \right]. \quad (\text{A.1})$$

Bibliography

- [1] T. Abbott, Y. Akiba, D. Alburger, D. Beavis, R. R. Betts, L. Birstein, M. A. Bloomer, P. D. Bond, C. Chasman, Y. Y. Chu, B. A. Cole, J. B. Costales, H. J. Crawford, J. B. Cumming, R. Debbé, E. Duek, J. Engelage, S. Y. Fung, L. Grodzins, S. Gushue, H. Hamagaki, O. Hansen, S. Hayashi, S. Homma, H. Z. Huang, Y. Ikeda, S. Katcoff, S. Kaufman, K. Kimura, K. Kitamura, K. Kurita, R. J. Ledoux, M. J. Levine, Y. Miake, R. J. Morse, S. Nagamiya, J. Olness, C. G. Parsons, L. P. Remsberg, M. Sarabura, A. Shor, P. Stankus, S. G. Steadman, G. S. F. Stephans, T. Sugitate, M. J. Tannenbaum, M. Torikoshi, J. H. van Dijk, F. Videbaek, M. Vient, P. Vincent, E. Vulgaris, V. Vutsadakis, W. A. Watson, H. E. Wegner, D. S. Woodruff, Y. D. Wu, and W. A. Zajc. Kaon and pion production in central si+au collisions at 14.6 A gev/ c . *Phys. Rev. Lett.*, 64:847–850, Feb 1990.
- [2] B. I. Abelev, M. M. Aggarwal, Z. Ahammed, B. D. Anderson, M. Anderson, D. Arkhipkin, G. S. Averichev, Y. Bai, J. Balewski, O. Barannikova, L. S. Barnby, J. Baudot, S. Bekele, V. V. Belaga, A. Bellingeri-Laurikainen, R. Bellwied, F. Benedosso, S. Bhardwaj, A. Bhasin, A. K. Bhati, H. Bichsel, J. Bielcik, J. Bielcikova, L. C. Bland, S-L. Blyth, B. E. Bonner, M. Botje, J. Bouchet, A. V. Brandin, A. Bravar, T. P. Burton, M. Bystersky, R. V. Cadman, X. Z. Cai, H. Caines, M. Calderón de la Barca Sánchez, J. Castillo, O. Catu, D. Cebra, Z. Chajecki, P. Chaloupka, S. Chattopadhyay, H. F. Chen, J. H. Chen, J. Cheng, M. Cherney, A. Chikanian, W. Christie, J. P. Coffin, T. M. Cormier, M. R. Cosentino, J. G. Cramer, H. J. Crawford, D. Das, S. Das, S. Dash, M. Daugherty, M. M. de Moura, T. G. Dedovich, M. DePhillips, A. A. Derevschikov, L. Didenko, T. Dietel, P. Djawotho, S. M. Dogra, W. J. Dong, X. Dong, J. E. Draper, F. Du, V. B. Dunin, J. C. Dunlop, M. R. Dutta Mazumdar, V. Eckardt, W. R. Edwards, L. G. Efimov, V. Emelianov, J. Engelage, G. Eppley, B. Erasmus, M. Estienne, P. Fachini, R. Fatemi, J. Fedorisin, P. Filip, E. Finch, V. Fine, Y. Fisyak, J. Fu, C. A. Gagliardi, L. Gaillard, M. S. Ganti, V. Ghazikhanian, P. Ghosh, J. E. Gonzalez, Y. G. Gorbunov, H. Gos, O. Grebenyuk, D. Grosnick, S. M. Guertin, K. S. F. F. Guimaraes, N. Gupta, T. D. Gutierrez, B. Haag, T. J. Hallman, A. Hamed, J. W. Harris, W. He, M. Heinz, T. W. Henry, S. Hepplemann, B. Hippolyte, A. Hirsch, E. Hjort, A. M. Hoffman, G. W. Hoffmann, M. J. Horner, H. Z. Huang, S. L. Huang, E. W. Hughes, T. J. Humanic, G. Igo, P. Jacobs, W. W. Jacobs, P. Jakl, F. Jia, H. Jiang, P. G. Jones, E. G. Judd, S. Kabana, K. Kang, J. Kapitan, M. Kaplan, D. Keane, A. Kechechyan, V. Yu. Khodyrev, B. C. Kim, J. Kiryluk, A. Kisiel, E. M. Kislov, S. R. Klein, A. Kocoloski, D. D. Koetke, T. Kollegger, M. Kopytine, L. Kotchenda,

V. Kouchpil, K. L. Kowalik, M. Kramer, P. Kravtsov, V. I. Kravtsov, K. Krueger, C. Kuhn, A. I. Kulikov, A. Kumar, A. A. Kuznetsov, M. A. C. Lamont, J. M. Landgraf, S. Lange, S. LaPointe, F. Laue, J. Lauret, A. Lebedev, R. Lednicky, C-H. Lee, S. Lehocka, M. J. LeVine, C. Li, Q. Li, Y. Li, G. Lin, X. Lin, S. J. Lindenbaum, M. A. Lisa, F. Liu, H. Liu, J. Liu, L. Liu, Z. Liu, T. Ljubicic, W. J. Llope, H. Long, R. S. Longacre, W. A. Love, Y. Lu, T. Ludlam, D. Lynn, G. L. Ma, J. G. Ma, Y. G. Ma, D. Magestro, D. P. Mahapatra, R. Majka, L. K. Mangotra, R. Manweiler, S. Margetis, C. Markert, L. Martin, H. S. Matis, Yu. A. Matulenko, C. J. McClain, T. S. McShane, Yu. Melnick, A. Meschanin, J. Millane, M. L. Miller, N. G. Minaev, S. Mioduszewski, C. Mironov, A. Mischke, D. K. Mishra, J. Mitchell, B. Mohanty, L. Molnar, C. F. Moore, D. A. Morozov, M. G. Munhoz, B. K. Nandi, C. Nattrass, T. K. Nayak, J. M. Nelson, N. S. Nepali, P. K. Netrakanti, L. V. Nogach, S. B. Nurushev, G. Odyniec, A. Ogawa, V. Okorokov, M. Oldenburg, D. Olson, M. Pachr, S. K. Pal, Y. Panebratsev, S. Y. Panitkin, A. I. Pavlinov, T. Pawlak, T. Peitzmann, V. Perevoztchikov, C. Perkins, W. Peryt, S. C. Phatak, R. Picha, M. Planinic, J. Pluta, N. Poljak, N. Porile, J. Porter, A. M. Poskanzer, M. Potekhin, E. Potrebenikova, B. V. K. S. Potukuchi, D. Prindle, C. Pruneau, J. Putschke, G. Rakness, R. Raniwala, S. Raniwala, R. L. Ray, S. V. Razin, J. Reinnarth, D. Relyea, A. Ridiger, H. G. Ritter, J. B. Roberts, O. V. Rogachevskiy, J. L. Romero, A. Rose, C. Roy, L. Ruan, M. J. Russcher, R. Sahoo, T. Sakuma, S. Salur, J. Sandweiss, M. Sarsour, P. S. Sazhin, J. Schambach, R. P. Scharenberg, N. Schmitz, J. Seger, I. Selyuzhenkov, P. Seyboth, A. Shabetai, E. Shaliev, M. Shao, M. Sharma, W. Q. Shen, S. S. Shimanskiy, E. P. Sichtermann, F. Simon, R. N. Singaraju, N. Smirnov, R. Snellings, G. Sood, P. Sorensen, J. Sowinski, J. Speltz, H. M. Spinka, B. Srivastava, A. Stadnik, T. D. S. Stanislaus, R. Stock, A. Stolpovsky, M. Strikhanov, B. Stringfellow, A. A. P. Suaide, N. L. Subba, E. Sugarbaker, M. Sumner, Z. Sun, B. Surrow, M. Swanger, T. J. M. Symons, A. Szanto de Toledo, A. Tai, J. Takahashi, A. H. Tang, T. Tarnowsky, D. Thein, J. H. Thomas, A. R. Timmins, S. Timoshenko, M. Tokarev, T. A. Trainor, S. Trentalange, R. E. Tribble, O. D. Tsai, J. Ulery, T. Ullrich, D. G. Underwood, G. Van Buren, N. van der Kolk, M. van Leeuwen, A. M. Vander Molen, R. Varma, I. M. Vasilevski, A. N. Vasiliev, R. Vernet, S. E. Vigdor, Y. P. Viyogi, S. Vokal, S. A. Voloshin, W. T. Waggoner, F. Wang, G. Wang, J. S. Wang, X. L. Wang, Y. Wang, J. W. Watson, J. C. Webb, G. D. Westfall, A. Wetzler, C. Whitten, H. Wieman, S. W. Wissink, R. Witt, J. Wood, J. Wu, N. Xu, Q. H. Xu, Z. Xu, P. Yepes, I-K. Yoo, V. I. Yurevich, W. Zhan, H. Zhang, W. M. Zhang, Y. Zhang, Z. P. Zhang, Y. Zhao, C. Zhong, R. Zoukarnneev, Y. Zoukarnneeva, A. N. Zubarev, and J. X. Zuo. Identified baryon and meson distributions at large transverse momenta from Au + Au collisions at $\sqrt{s_{NN}} = 200$ GeV. *Phys. Rev. Lett.*, 97:152301, Oct 2006.

- [3] M. C. Abreu et al. Evidence for deconfinement of quarks and gluons from the J / ψ suppression pattern measured in Pb + Pb collisions at the CERN SPS. *Phys. Lett.*, B477:28–36, 2000.
- [4] A. Adare, S. Afanasiev, C. Aidala, N. N. Ajitanand, Y. Akiba, H. Al-Bataineh, J. Alexander, A. Angerami, K. Aoki, N. Apadula, Y. Aramaki, E. T. Atomssa, R. Aver-

beck, T. C. Awes, B. Azmoun, V. Babintsev, M. Bai, G. Baksay, L. Baksay, K. N. Barish, B. Bassalleck, A. T. Basye, S. Bathe, V. Baublis, C. Baumann, A. Bazilevsky, S. Belikov, R. Belmont, R. Bennett, A. Berdnikov, Y. Berdnikov, J. H. Bhom, A. A. Bickley, D. S. Blau, J. S. Bok, K. Boyle, M. L. Brooks, H. Buesching, V. Bumazhnov, G. Bunce, S. Butsyk, C. M. Camacho, S. Campbell, A. Caringi, C.-H. Chen, C. Y. Chi, M. Chiu, I. J. Choi, J. B. Choi, R. K. Choudhury, P. Christiansen, T. Chujo, P. Chung, O. Chvala, V. Cianciolo, Z. Citron, B. A. Cole, Z. Conesa del Valle, M. Connors, P. Constantin, M. Csanád, T. Csörgő, T. Dahms, S. Dairaku, I. Danchev, K. Das, A. Datta, G. David, M. K. Dayananda, A. Denisov, A. Deshpande, E. J. Desmond, K. V. Dharmawardane, O. Dietzsch, A. Dion, M. Donadelli, O. Drapier, A. Drees, K. A. Drees, J. M. Durham, A. Durum, D. Dutta, L. D'Orazio, S. Edwards, Y. V. Efremenko, F. Ellinghaus, T. Engelmores, A. Enokizono, H. En'yo, S. Esumi, B. Fadem, D. E. Fields, M. Finger, M. Finger, F. Fleuret, S. L. Fokin, Z. Fraenkel, J. E. Frantz, A. Franz, A. D. Frawley, K. Fujiwara, Y. Fukao, T. Fusayasu, I. Garishvili, A. Glenn, H. Gong, M. Gonin, Y. Goto, R. Granier de Cassagnac, N. Grau, S. V. Greene, G. Grim, M. Grosse Perdekamp, T. Gunji, H.-Å. Gustafsson, J. S. Haggerty, K. I. Hahn, H. Hamagaki, J. Hamblen, R. Han, J. Hanks, E. P. Hartouni, E. Haslum, R. Hayano, X. He, M. Heffner, T. K. Hemmick, T. Hester, J. C. Hill, M. Hohlmann, W. Holzmann, K. Homma, B. Hong, T. Horaguchi, D. Hornback, S. Huang, T. Ichihara, R. Ichimiya, J. Ide, Y. Ikeda, K. Imai, M. Inaba, D. Isenhower, M. Ishihara, T. Isobe, M. Issah, A. Isupov, D. Ivanischev, Y. Iwanaga, B. V. Jacak, J. Jia, X. Jiang, J. Jin, B. M. Johnson, T. Jones, K. S. Joo, D. Jouan, D. S. Jumper, F. Kajihara, S. Kametani, N. Kamihara, J. Kamin, J. H. Kang, J. Kapustinsky, K. Karatsu, M. Kasai, D. Kawall, M. Kawashima, A. V. Kazantsev, T. Kempel, A. Khanzadeev, K. M. Kijima, J. Kikuchi, A. Kim, B. I. Kim, D. H. Kim, D. J. Kim, E. Kim, E.-J. Kim, S. H. Kim, Y.-J. Kim, E. Kinney, K. Kiriluk, Á. Kiss, E. Kistenev, D. Kleinjan, L. Kochenda, B. Komkov, M. Konno, J. Koster, D. Kotchetkov, A. Kozlov, A. Král, A. Kravitz, G. J. Kunde, K. Kurita, M. Kurosawa, Y. Kwon, G. S. Kyle, R. Lacey, Y. S. Lai, J. G. Lajoie, A. Lebedev, D. M. Lee, J. Lee, K. Lee, K. B. Lee, K. S. Lee, M. J. Leitch, M. A. L. Leite, E. Leitner, B. Lenzi, X. Li, P. Lichtenwalner, P. Liebing, L. A. Linden Levy, T. Liška, A. Litvinenko, H. Liu, M. X. Liu, B. Love, R. Luechtenborg, D. Lynch, C. F. Maguire, Y. I. Makdisi, A. Malakhov, M. D. Malik, V. I. Manko, E. Mannel, Y. Mao, H. Masui, F. Matathias, M. McCumber, P. L. McGaughey, D. McGlinchey, N. Means, B. Meredith, Y. Miake, T. Mibe, A. C. Mignerey, P. Mikeš, K. Miki, A. Milov, M. Mishra, J. T. Mitchell, A. K. Mohanty, H. J. Moon, Y. Morino, A. Morreale, D. P. Morrison, T. V. Moukhanova, T. Murakami, J. Murata, S. Nagamiya, J. L. Nagle, M. Naglis, M. I. Nagy, I. Nakagawa, Y. Nakamiya, K. R. Nakamura, T. Nakamura, K. Nakano, S. Nam, J. Newby, M. Nguyen, M. Nihashi, R. Nouicer, A. S. Nyanin, C. Oakley, E. O'Brien, S. X. Oda, C. A. Ogilvie, M. Oka, K. Okada, Y. Onuki, A. Oskarsson, M. Ouchida, K. Ozawa, R. Pak, V. Pantuev, V. Papavassiliou, I. H. Park, J. Park, S. K. Park, W. J. Park, S. F. Pate, H. Pei, J.-C. Peng, H. Pereira, V. Peresedov, D. Yu. Peressounko, R. Petti, C. Pinkenburg, R. P. Pisani, M. Proissl, M. L. Purschke, A. K. Purwar, H. Qu, J. Rak, A. Rakotozafindrabe, I. Ravinovich, K. F. Read, S. Rembeczki, K. Reygers, V. Riabov, Y. Riabov, E. Richardson, D. Roach, G. Roche, S. D. Rolnick, M. Rosati,

- C. A. Rosen, S. S. E. Rosendahl, P. Rosnet, P. Rukoyatkin, P. Ružička, B. Sahlmueller, N. Saito, T. Sakaguchi, K. Sakashita, V. Samsonov, S. Sano, T. Sato, S. Sawada, K. Sedgwick, J. Seele, R. Seidl, A. Yu. Semenov, R. Seto, D. Sharma, I. Shein, T.-A. Shibata, K. Shigaki, M. Shimomura, K. Shoji, P. Shukla, A. Sickles, C. L. Silva, D. Silvermyr, C. Silvestre, K. S. Sim, B. K. Singh, C. P. Singh, V. Singh, M. Slunečka, R. A. Soltz, W. E. Sondheim, S. P. Sorensen, I. V. Sourikova, N. A. Sparks, P. W. Stankus, E. Stenlund, S. P. Stoll, T. Sugitate, A. Sukhanov, J. Sziklai, E. M. Takagui, A. Taketani, R. Tanabe, Y. Tanaka, S. Taneja, K. Tanida, M. J. Tannenbaum, S. Tarafdar, A. Taranenko, P. Tarján, H. Themann, D. Thomas, T. L. Thomas, M. Togawa, A. Toia, L. Tomášek, H. Torii, R. S. Towell, I. Tserruya, Y. Tsuchimoto, C. Vale, H. Valle, H. W. van Hecke, E. Vazquez-Zambrano, A. Veicht, J. Velkovska, R. Vértesi, A. A. Vinogradov, M. Virius, V. Spectra and ratios of identified particles in au+au and d+au collisions at $\sqrt{s_{NN}} = 200$ gev. *Phys. Rev. C*, 88:024906, Aug 2013.
- [5] K. Adcox et al. Formation of dense partonic matter in relativistic nucleus-nucleus collisions at RHIC: Experimental evaluation by the PHENIX collaboration. *Nucl. Phys.*, A757:184–283, 2005.
 - [6] A. Akindinov et al. The multigap resistive plate chamber as a time-of-flight detector. *Nucl. Instrum. Meth.*, A456:16–22, 2000.
 - [7] D. M. Alde, H. W. Baer, T. A. Carey, G. T. Garvey, A. Klein, C. Lee, M. J. Leitch, J. W. Lillberg, P. L. McGaughey, C. S. Mishra, J. M. Moss, J. C. Peng, C. N. Brown, W. E. Cooper, Y. B. Hsiung, M. R. Adams, R. Guo, D. M. Kaplan, R. L. McCarthy, G. Danner, M. J. Wang, M. L. Barlett, and G. W. Hoffmann. Nuclear dependence of the production of Υ resonances at 800 gev. *Phys. Rev. Lett.*, 66:2285–2288, May 1991.
 - [8] F. Antinori et al. Production of strange and multistrange hadrons in nucleus nucleus collisions at the SPS. *Nucl. Phys.*, A661:130–139, 1999.
 - [9] Jean Barrette. Anisotropic azimuthal distributions of identified particles in Au + Au collisions at 11.5/A-GeV/c. *Nucl. Phys.*, A661:329–332, 1999.
 - [10] CAD @ BNL. Rhic accelerators. *BNL website*, July 2016.
 - [11] Peter Braun-Munzinger and Johanna Stachel. Dynamics of ultrarelativistic nuclear collisions with heavy beams: An Experimental overview. *Nucl. Phys.*, A638:3–18, 1998.
 - [12] Henner Buesching. The electromagnetic calorimeter. *FOCUS Talk*, February 2003.
 - [13] Sergey Butsyk. Phenix drift chamber operation principles. *FOCUS Talk*, January 2003.
 - [14] Mickey Chiu. Phenix focus: Zero degree calorimeter. *FOCUS Talk*, December 2003.
 - [15] John C. Collins and M. J. Perry. Superdense Matter: Neutrons Or Asymptotically Free Quarks? *Phys. Rev. Lett.*, 34:1353, 1975.

- [16] M. D. Corcoran et al. Evidence for multiple scattering of high-energy partons in nuclei. *Phys. Lett.*, B259:209–215, 1991.
- [17] J. W. Cronin, H. J. Frisch, M. J. Shochet, J. P. Boymond, P. A. Piroué, and R. L. Sumner. Production of hadrons at large transverse momentum at 200, 300, and 400 gev. *Phys. Rev. D*, 11:3105–3123, Jun 1975.
- [18] Sidney D. Drell and Tung-Mow Yan. Massive lepton-pair production in hadron-hadron collisions at high energies. *Phys. Rev. Lett.*, 25:316–320, Aug 1970.
- [19] A. Pikin et al. Rhic ebis: basics of design and status of commissioning. *Journal of Instrumentation*, 5(C09003), September 2010.
- [20] T. Fields and M. D. Corcoran. Nuclear rescattering effects in massive dihadron production. *Phys. Rev. Lett.*, 70:143–145, Jan 1993.
- [21] K.F. Read for PHENIX collab. *15th Winter Workshop on Nuclear Dynamics*, Park City, Utah, January 1999.
- [22] Tarun Kanti Ghosh, K. Adcox, S. S. Adler, N. Ajitanand, Y. Akiba, J. Alexander, L. Aphecetche, Y. Arai, S. H. Aronson, R. Averbeck, T. C. Awes, K. N. Barish, P. D. Barnes, J. Barrette, B. Bassalleck, S. Bathe, V. Baublis, A. Bazilevsky, S. Belikov, F. G. Bellaiche, S. T. Belyaev, M. J. Bennett, Y. Berdnikov, S. Botelho, M. L. Brooks, D. S. Brown, N. Bruner, D. Bucher, H. Buesching, V. Bumazhnov, G. Bunce, J. Burward-Hoy, S. Butsyk, T. A. Carey, P. Chand, J. Chang, W. C. Chang, L. L. Chavez, S. Chernichenko, C. Y. Chi, J. Chiba, M. Chiu, R. K. Choudhury, T. Christ, T. Chujo, M. S. Chung, P. Chung, V. Cianciolo, B. A. Cole, D. G. D’Enterria, G. David, H. Delagrange, A. Denisov, A. Deshpande, E. J. Desmond, O. Dietzsch, B. V. Dinesh, A. Drees, A. Durum, D. Dutta, K. Ebisu, Y. V. Efremenko, K. El Chenawi, H. En’yo, S. Esumi, L. Ewell, T. Ferdousi, D. E. Fields, S. L. Fokin, Z. Fraenkel, A. Franz, A. D. Frawley, S-Y Fung, S. Garpman, T. K. Ghosh, A. Glenn, A. L. Godoi, Y. Goto, S. V. Greene, M. Grosse Perdekamp, S. K. Gupta, W. Guryn, H-Å Gustafsson, J. S. Haggerty, H. Hamagaki, A. G. Hansen, H. Hara, E. P. Hartouni, R. Hayano, N. Hayashi, X. He, T. K. Hemmick, J. Heuser, J. C. Hill, D. S. Ho, K. Homma, B. Hong, A. Hoover, T. Ichihara, K. Imai, M. S. Ippolitov, M. Ishihara, B. V. Jacak, W. Y. Jang, J. Jia, B. M. Johnson, S. C. Johnson, K. S. Joo, S. Kametani, J. H. Kang, M. Kann, S. S. Kapoor, S. Kelly, B. Khachaturov, A. Khanzadeev, J. Kikuchi, D. J. Kim, H. J. Kim, S. Y. Kim, Y. G. Kim, W. W. Kinnison, E. Kistenev, A. Kiyomichi, C. Klein-Boesing, S. Klinksiek, L. Kochenda, D. Kochetkov, V. Kochetkov, D. Koehler, T. Kohama, A. Kozlov, P. J. Kroon, K. Kurita, M. J. Kweon, Y. Kwon, G. S. Kyle, R. Lacey, J. G. Lajoie, J. Lauret, A. Lebedev, D. M. Lee, M. J. Leitch, X. H. Li, Z. Li, D. J. Lim, M. X. Liu, X. Liu, Z. Liu, C. F. Maguire, J. Mahon, Y. I. Makdisi, V. I. Manko, Y. Mao, S. K. Mark, S. Markacs, G. Martinez, M. D. Marx, A. Masaike, F. Matathias, T. Matsumoto, P. L. McGaughey, E. Melnikov, M. Merschmeier, F. Messer, M. Messer, Y. Miake, T. E. Miller, A. Milov, S. Mioduszewski, R. E. Mischke, G. C. Mishra, J. T. Mitchell, A. K. Mohanty, D. P. Morrison, J. M. Moss, F. Mühlbacher, M. Muniruz-zaman, J. Murata, S. Nagamiya, Y. Nagasaka, J. L. Nagle, Y. Nakada, B. K. Nandi,

- J. Newby, L. Nikkinen, P. Nilsson, S. Nishimura, A. S. Nyanin, J. Nystrand, E. O'Brien, C. A. Ogilvie, H. Ohnishi, I. D. Ojha, M. Ono, V. Onuchin, A. Oskarsson, L. Österman, I. Otterlund, K. Oyama, L. Paffrath, A. P. T. Palounek, V. S. Pantuev, V. Papavassiliou, S. F. Pate, T. Peitzmann, A. N. Petridis, C. Pinkenburg, R. P. Pisani, P. Pitukhin, F. Plasil, M. Pollack, K. Pope, M. L. Purschke, I. Ravinovich, K. F. Read, K. Reygers, V. Riabov, Y. Riabov, M. Rosati, A. A. Rose, S. S. Ryu, N. Saito, A. Sakaguchi, T. Sakaguchi, H. Sako, T. Sakuma, V. Samsonov, T. C. Sangster, R. Santo, H. D. Sato, S. Sato, S. Sawada, B. R. Schlei, Y. Schutz, V. Semenov, R. Seto, T. K. Shea, I. Shein, T-A Shibata, K. Shigaki, T. Shiina, Y. H. Shin, I. G. Sibirak, D. Silvermyr, K. S. Sim, J. Simon-Gillo, C. P. Singh, V. Singh, M. Sivertz, A. Soldatov, R. A. Soltz, S. Sorensen, P. W. Stankus, N. Starinsky, P. Steinberg, E. Stenlund, A. Ster, S. P. Stoll, M. Sugioka, T. Sugitate, J. P. Sullivan, Y. Sumi, Z. Sun, M. Suzuki, E. M. Takagui, A. Taketani, M. Tamai, K. H. Tanaka, Y. Tanaka, E. Taniguchi, M. J. Tannenbaum, J. Thomas, J. H. Thomas, T. L. Thomas, W. Tian, J. Tojo, H. Torii, R. S. Towell, I. Tserruya, H. Tsuruoka, A. A. Tsvetkov, S. K. Tuli, H. Tydesjö, N. Tyurin, T. Ushiroda, H. W. van Hecke, C. Velissaris, J. Velkovska, M. Velkovsky, A. A. Vinogradov, M. A. Volkov, A. Vorobyov, E. Vznuzdaev, H. Wang, Y. Watanabe, S. N. White, C. Witzig, F. K. Wohn, C. L. Woody, W. Xie, and etal. First results from rhic-phenix. *Pramana*, 57(2):355–369, 2001.
- [23] Judy Goldhaber. Bevalac had 40-year record of historic discoveries. *Berkeley Lab Science Articles Archive*, October 1992.
- [24] H. A. Gustafsson, H. H. Gutbrod, B. Kolb, H. Löhner, B. Ludewigt, A. M. Poskanzer, T. Renner, H. Riedesel, H. G. Ritter, A. Warwick, F. Weik, and H. Wieman. Collective flow observed in relativistic nuclear collisions. *Phys. Rev. Lett.*, 52:1590–1593, Apr 1984.
- [25] Ulrich W. Heinz and Barbara V. Jacak. Two particle correlations in relativistic heavy ion collisions. *Ann. Rev. Nucl. Part. Sci.*, 49:529–579, 1999.
- [26] C. Hohne. Strangeness production in nuclear collisions: Recent results from experiment NA49. *Nucl. Phys.*, A661:485–488, 1999.
- [27] Rudolph C. Hwa and C. B. Yang. Final-state interaction as the origin of the cronin effect. *Phys. Rev. Lett.*, 93:082302, Aug 2004.
- [28] Rudolph C. Hwa and C. B. Yang. Recombination of shower partons at high p_T in heavy-ion collisions. *Phys. Rev. C*, 70:024905, Aug 2004.
- [29] Akio Kiyomichi. PHENIX internal analysis notes, 2002.
- [30] David William Kleinjan. *Measurement of the Transverse Single Spin Asymmetry and the Invariant Cross Section of Inclusive Eta Mesons Produced from Transversely Polarized Proton-Proton Collisions at Center of Mass Energy of 200 GeV*. PhD thesis, University of California, Riverside, 2014.
- [31] J. H. Kühn. Nucleon-number dependence of large-transverse-momentum reactions and multiple scattering. *Phys. Rev. D*, 13:2948–2953, Jun 1976.

- [32] J. M. Brennan M. Blaskiewicz and K. Mernick. Three-dimensional stochastic cooling in the relativistic heavy ion collider. *Phys. Rev. Lett.*, 105(094801), August 2010.
- [33] Hiroshi Masui. Phenix focus: Time of flight. *FOCUS Talk*, February 2004.
- [34] J. T. Mitchell et al. Event reconstruction in the PHENIX central arm spectrometers. *Nucl. Instrum. Meth.*, A482:491–512, 2002.
- [35] Anders Oskarsson. The pad chambers. *FOCUS Talk*, January 2003.
- [36] ARTHUR L. ROBINSON. Nuclear squeeze at lawrence berkeley lab. *Science*, 224(4651):857–858, 1984.
- [37] Edward V. Shuryak. Quantum Chromodynamics and the Theory of Superdense Matter. *Phys. Rept.*, 61:71–158, 1980.
- [38] Lucas Taylor. Resistive plate chambers. *CMS Detectors Web Page*, November 2011.
- [39] Alberica Toia. Participants and spectators at the heavy-ion fireball. *CERN Courier*, April 2013.
- [40] Sebastian White. RHIC/PHENIX hosted group page, 2003.
- [41] F. Wojciech. *Phenomenology of Ultra-relativistic Heavy-ion Collisions*. World Scientific.